arXiv:2504.18526v1 [math.NA] 25 Apr 2025

ROBUST SEMI-IMPLICIT MULTILEVEL SDC METHODS FOR CONSERVATION LAWS

ERIK PFISTER, JÖRG STILLER

Abstract. Semi-implicit multilevel spectral deferred correction (SI-MLSDC) methods provide a promising approach for high-order time integration for nonlinear evolution equations including conservation laws. However, existing methods lack robustness and often do not achieve the expected advantage over single-level SDC. This work adopts the novel SI time integrators from [44] for enhanced stability and extends the single-level SI-SDC method with a multilevel approach to increase computational efficiency. The favourable properties of the resulting SI-MLSDC method are shown by linear temporal stability analysis for a convection-diffusion problem. The robustness and efficiency of the fully discrete method involving a high-order discontinuous Galerkin SEM discretization are demonstrated through numerical experiments for the convection–diffusion, Burgers, Euler and Navier–Stokes equations. The method is shown to yield substantial reductions in fine-grid iterations compared to single-level SI-SDC across a broad range of test cases. Finally, current limitations of the SI-MLSDC framework are identified and discussed, providing guidance for future improvements.

1. Introduction

The use of higher-order numerical methods for conservation laws in fluid mechanics and related areas has increased significantly due to their superior convergence properties. Consequently, there is a corresponding need for time integration schemes that match these convergence rates and efficiency of spatial discretization techniques. This is essential to prevent an imbalance when solving partial differential equations (PDEs), where spatial and temporal errors should scale appropriately. The objective is to develop time integration schemes that enable the stable solution of PDEs with arbitrarily high order in both space and time. During the past decades, this challenge has led to the development of various high-order methods, including explicit, implicit, and semi-implicit schemes incorporating multiple steps or stages [18], [20], [19]. Explicit time integration methods become increasingly inefficient as stiffness increases, which is often the case in the presence of unresolved waves, diffusion, or local mesh refinement. This issue is particularly pronounced in high-order spatial finite element methods. To overcome the restrictive time step limitations imposed by stiffness, one strategy is to utilize fully implicit methods, such as diagonally implicit Runge-Kutta methods [26], [34], [35], Rosenbrock methods [4], Taylor methods [3] or discontinuous Galerkin methods in time [45]. Unfortunately, these fully implicit methods frequently result in ill-conditioned algebraic systems that are costly to solve, making it challenging for them to compete with explicit methods in time-resolved simulations. Semi-implicit methods handle non-stiff convection explicitly and stiff diffusion implicitly, resulting in manageable algebraic systems using standard linear algebra. Common techniques include IMEX multistep and Runge-Kutta methods, balancing efficiency and stability. In practice, however, IMEX multistep methods typically do not exceed an order of 3 [16], [24], [27]. A more favourable alternative is the use of

TU Dresden, Institute of Fluid Mechanics, 01062 Dresden, Germany

E-mail address: erik.pfister@tu-dresden.de.

Key words and phrases. Semi-implicit methods; Spectral deferred correction; discontinuous Galerkin method; Multilevel space-time method .

IMEX Runge-Kutta methods, which offer improved stability properties and lower error constants [2], [8], [25].

Recently, significant advances have been made in the development of higher-order semi-implicit time integration methods through the use of multi-derivative techniques [17], [38]. Another promising approach is the use of spectral deferred correction (SDC) methods, which enable the construction of time integration schemes with arbitrarily high order [13]. Semi-implicit spectral deferred correction (SI-SDC) methods were introduced [32] and have since undergone further evolvement [9], [10], [30], [43]. The semi-implicit SDC methods proposed in [44] even proof to be L-stable up to order 11. However, a key challenge with these SDC methods is the relatively large number of iterations required to achieve convergence, highlighting the need for techniques that enhance convergence efficiency.

So-called Ladder methods, as referenced in [29], [32], initiate with fewer substeps in early SDC iterations to align with the solution's accuracy, gradually advancing from a coarse, low-order solution to a refined, high-order one. These methods employ one or more SDC sweeps at a coarse level, then interpolate the outcome in both time and space to serve as the provisional solution for subsequent correction sweeps. The authors conclude however, that while ladder methods reduce workload, this benefit is counterbalanced by a decrease in accuracy, resulting in no computational efficiency gains. In [29], the results indicate that this problem can be overcome, if the ladder methods allow both spatial and temporal coarsening. An extension of this concept involves employing a general multilevel strategy, following Brandt and Livne [6] in the context of SDC methods, as demonstrated by Speck et al. [42]. A comparable approach is implemented in the Parallel Full Approximation Scheme in Space and Time (PFASST) [14], [31], [5] or [37]. Kremling and Speck [28] proved the convergence of multilevel SDC (MLSDC) and examined the role of the coarsening strategy. Furthermore, Hamon et al. [21] introduced an IMEX MLSDC method for the shallow water equations with a spatial discretization based on the global Spherical Harmonics transform. Finally, Emmett et al. [15] developed an adaptive MLSDC approach applied to the Navier-Stokes equations, representing another step toward enhancing runtime. However, it presents an explicit treatment of convection and diffusion and is restricted to an order of four in space and time.

This paper develops a novel SI-MLSDC method that extends the single-level SDC method proposed in [44] and thereby achieves vastly improved stability properties compared to existing SI-MLSDC methods. Furthermore, earlier studies focus on spatial discretizations based on finite difference or finite volume methods, while high-order discontinuous Galerkin spectral element methods (DG-SEM) have received comparatively little attention in this context. Additionally, no prior work known to the authors systematically investigates the influence of starting strategies to the MLSDC algorithm and the influence of the transfer operators. Moreover, none of the aforementioned works utilize embedded interpolation as a projection method, which is feasible in our approach due to the availability of spatial and temporal basis functions. In addition, the distinction between incremental and non-incremental MLSDC formulations has also not been explicitly explored. Most importantly, none of the existing studies incorporate the novel semi-implicit (SI) time integrators from [44] that offer enhanced stability properties. The approach presented here introduces a highly stable and robust SI-MLSDC scheme combined with DG-SEM for conservation laws, enabling p-coarsening in time as well as simultaneous p- and h-coarsening in space, thereby addressing these gaps - while also critically examining current limitations of MLSDC. The paper is structured as followed: Section 2 provides a concise overview of the one-dimensional conservation laws under consideration. Section 3 and 4 present the proposed SI-SDC and SI-MLSDC methods, followed by an investigation of the stability properties of the methods with a linear stability analysis of the convection-diffusion problem in Section 5. Spatial discretization, including

stabilization techniques, is described in Section 6. Section 7 provides preliminary studies for the application of the SI-MLSDC method to partial differential equations and Section 8 extends the studies by onvection-diffusion, Burgers, and compressible flow problems. A summary of findings is provided in Section 9.

2. Problem

A system of conservation laws for the variables $\boldsymbol{u}(x,t) \in \mathbb{R}^d$, governed by the equation

$$\partial_t \boldsymbol{u} + \partial_x \boldsymbol{f}_{\mathrm{c}}(\boldsymbol{u}) = \partial_x \boldsymbol{f}_{\mathrm{d}}(\boldsymbol{u}) + \boldsymbol{f}_{\mathrm{s}}(\boldsymbol{u}, x, t) \tag{1}$$

is considered where $x \in \Omega \subset \mathbb{R}$ and $t \in \mathbb{R}^+$. The vector $\boldsymbol{u}(x,t) \in \mathbb{R}^d$ represents the conserved quantities, $\boldsymbol{f}_{\mathrm{c}}$ denotes the convective fluxes, $\boldsymbol{f}_{\mathrm{d}}$ represents the diffusive fluxes, and $\boldsymbol{f}_{\mathrm{s}}$ accounts for any source terms. By introducing the combined right-hand side

$$\boldsymbol{f} = -\partial_x \boldsymbol{f}_{\mathrm{c}} + \partial_x \boldsymbol{f}_{\mathrm{d}} + \boldsymbol{f}_{\mathrm{s}}\,, \tag{2}$$

the system can be rewritten in the following evolutionary form:

$$\partial_t \boldsymbol{u} = \boldsymbol{f}(\boldsymbol{u}, x, t)\,. \tag{3}$$

It is assumed that the convective fluxes possess the Jacobian $\boldsymbol{A}_{\mathrm{c}} = \boldsymbol{f}_{\mathrm{c}}'(\boldsymbol{u})$ and the diffusive fluxes can be written in the form $\boldsymbol{f}_{\mathrm{d}} = \boldsymbol{A}_{\mathrm{d}} \partial_x \boldsymbol{u}$, where $\boldsymbol{A}_{\mathrm{d}}(\boldsymbol{u}, \partial_x \boldsymbol{u})$ is the positive-semidefinite diffusion matrix. These definitions yield the quasilinear form

$$\partial_t \boldsymbol{u} = -\boldsymbol{A}_{\mathrm{c}} \partial_x \boldsymbol{u} + \partial_x \boldsymbol{A}_{\mathrm{d}} \partial_x \boldsymbol{u} + \boldsymbol{f}_{\mathrm{s}}\,. \tag{4}$$

2.1. Scalar conservation laws. For these problems, the variable $\boldsymbol{u}$ consist only of one scalar component u. Two particular equations are of interest. The first is the convection-diffusion equation

$$\partial_t u = -\partial_x(vu) + \partial_x(\nu \partial_x u)\,, \tag{5}$$

where v is a constant velocity. The second case is the Burgers equation, which introduces nonlinear convection instead of a constant velocity and includes an additional source term. It is given by

$$\partial_t u = -\partial_x\left(\tfrac{1}{2}u^2\right) + \partial_x(\nu \partial_x u) + f_{\mathrm{s}}(x,t)\,, \tag{6}$$

where f_{s} represents a source term which could be tailored to match a specific solution. In both equations $\nu \geq 0$ is a constant diffusivity.

2.2. Euler and Navier-Stokes equations. For the Navier-Stokes equations, the conservative variables, convective fluxes and diffusive fluxes given by

$$\boldsymbol{u} = \begin{bmatrix} \rho \\ \rho v \\ \rho E \end{bmatrix}, \quad \boldsymbol{f}_{\mathrm{c}} = \begin{bmatrix} \rho v \\ \rho v^2 + p \\ \rho v E + p v \end{bmatrix}, \quad \boldsymbol{f}_{\mathrm{d}} = \begin{bmatrix} 0 \\ \frac{4}{3}\eta \partial_x v \\ \frac{4}{3}\eta v \partial_x v + \lambda \partial_x T \end{bmatrix}, \tag{7}$$

where ρ is the density, v the velocity, E the total specific energy, η the dynamic viscosity and λ the heat conductivity. Assuming a perfect gas with the gas constant $R = c_p - c_v$ and the ratio of the specific heats $\gamma = c_p/c_v$ it is possible to calculate the temperature $T = (E - v^2/2)/c_v$, the pressure

$p = \rho RT$, the total specific enthalpy $H = E + p/\rho$ and the speed of sound $a = ((\gamma - 1)RT)^{1/2}$. The convective Jacobian and the diffusion matrix are given by

$$\boldsymbol{A}_{\mathrm{c}} = \begin{bmatrix} 0 & 1 & 0 \\ \frac{1}{2}(\gamma-3)v^2 & (3-\gamma)v & \gamma - 1 \\ \frac{1}{2}(\gamma-1)v^3 - vH & H - (\gamma-1)v^2 & \gamma v \end{bmatrix} \tag{8}$$

and

$$\boldsymbol{A}_{\mathrm{d}} = \begin{bmatrix} 0 & 0 & 0 \\ -\frac{4}{3}\nu v & \frac{4}{3}\nu & 0 \\ -\left(\frac{4}{3}\nu - \gamma\kappa\right)v^2 - \gamma\kappa E & \left(\frac{4}{3}\nu - \gamma\kappa\right)v & \gamma\kappa \end{bmatrix}, \tag{9}$$

where $\nu = \eta/\rho$ is the kinematic viscosity and $\kappa = \lambda/(\rho c_p)$ the thermal diffusivity. The inviscid case with $\eta = \lambda = 0$ leads to the Euler equations for which $\boldsymbol{A}_{\mathrm{d}} = \boldsymbol{0}$.

3. Single-level collocation and SDC methods

3.1. Notation. Before discussing the numerical time integration methods in detail, we introduce the required notation. The fundamental necessity for the methods considered in this section is to subdivide the time interval $[t, t + \Delta t]$ using a set of collocation points $\{t_m\}_{m=1}^{M}$, such that

$$t = t_0 \leq t_1 < \cdots < t_m < \cdots < t_M = t + \Delta t. \tag{10}$$

Depending on the choice of collocation points, different integration properties can be achieved. The two point distributions used in this study are:

- Radau Right nodes: exclude the left endpoint.
- Lobatto nodes: include both endpoints.

The initial value of the solution is denoted by $\boldsymbol{u}_0 = \boldsymbol{u}(t_0)$, and the numerical solution at the collocation nodes is represented by $\boldsymbol{u}_m \approx \boldsymbol{u}(t_m)$ for $m = 1, \ldots, M$. Those nodal solutions, excluding the initial value $\boldsymbol{u}_0$, are grouped into a solution vector:

$$\underline{\boldsymbol{u}} = \left[\{\boldsymbol{u}_m\}_{m=1}^{M}\right]. \tag{11}$$

Remark 1. *$\mathcal{L}(\underline{\boldsymbol{u}}, t) = \sum_{m=1}^{M} \boldsymbol{u}_m \ell_m(t)$ is the Lagrange interpolant constructed through the collocation nodes t_m. The polynomials $\ell_m(t)$ serve as the basis functions.*

Since the methods under consideration are iterative, the solution at iteration k is denoted by $\boldsymbol{u}_m^k \approx \boldsymbol{u}(t_m)$. This notation will be used consistently throughout the following sections.

3.2. Incremental collocation method. The derivation of SDC starts from the Picard integral form of a generic Initial Value Problem. An approximation to this integral can be achieved by utilizing a quadrature formula:

$$\boldsymbol{u}_m = \boldsymbol{u}_{m-1} + \Delta t \sum_{i=1}^{M} w_{m,i}^{\mathrm{NN}} \boldsymbol{f}(\boldsymbol{u}_i, t_i), \quad m = 1, \ldots, M, \tag{12}$$

where the incremental integration weights are defined as

$$w_{m,i}^{\mathrm{NN}} = \int_{\tau_{m-1}}^{\tau_m} \ell_i(\tau)\mathrm{d}\tau. \tag{13}$$

Note that $\boldsymbol{u}_1 = \boldsymbol{u}_0$ for Lobatto points. The above formulation is also referred to as the *node-to-node* or incremental collocation method (CM), indicated by the NN superscript. Rewriting the collocation method in an operator form, we obtain:

$$\boldsymbol{F}_m^{\mathrm{NN}}(\underline{\boldsymbol{u}}) \equiv \boldsymbol{u}_m - \boldsymbol{u}_{m-1} - \Delta t \sum_{i=1}^{M} w_{m,i}^{\mathrm{NN}} \boldsymbol{f}(\boldsymbol{u}_i, t_i) = \boldsymbol{0}\,, \quad m = 1, \dots M. \tag{14}$$

Consequently, the collocation method can be interpreted as a system of equations:

$$\underline{\boldsymbol{F}}^{\mathrm{NN}}(\underline{\boldsymbol{u}}) = \underline{\boldsymbol{0}}. \tag{15}$$

This method is solved iteratively using the incremental SDC method, which is explained below.

3.3. Incremental SDC method. The SDC method serves as an iterative solver for the collocation problem through low-order substepping methods. Refer to [33], [32], [13], [43] for a detailed derivation. For the SDC scheme in this work, predictors and correctors are used, which can be one-staged or two-staged. The predictor is a low-order time integrator, stepping through the subinterval points m to provide the 0-th approximation to the solution $\boldsymbol{u}_m^0$. The specific time integration methods used in this work are the IMEX Euler and the one- and two-stage semi-implicit time integration methods SI(1) and SI(2) developed in [44]. The one-stage IMEX Euler predictor reads

$$\boldsymbol{u}_m^0 = \boldsymbol{u}_{m-1}^0 + \boldsymbol{H}^{\mathrm{EU}}(\boldsymbol{u}_{m-1}^0, \boldsymbol{u}_m^0, \Delta t_m)\,, \quad m = 1, \dots M. \tag{16}$$

Note that the superscript 0 is not an exponent, but an iteration count. Each iteration k is commonly referred to as a sweep. The term $\boldsymbol{H}_m \approx \int_{t_{m-1}}^{t_m} (-\partial_x \boldsymbol{f}_{\mathrm{c}} + \partial_x \boldsymbol{f}_{\mathrm{d}})\mathrm{d}t$ represents the low-order approximation of the integral over the m-th subinterval. For the IMEX Euler, it reads

$$\boldsymbol{H}^{\mathrm{EU}}(\boldsymbol{u}_a, \boldsymbol{u}_b, \Delta t_m) = \Delta t_m \left[-\partial_x \boldsymbol{f}_{\mathrm{c}}(\boldsymbol{u}_a) + \partial_x \boldsymbol{A}_{\mathrm{d}}(\boldsymbol{u}_a)\partial_x \boldsymbol{u}_b\right]. \tag{17}$$

The one-stage predictor SI(1) reads

$$\boldsymbol{u}_m^0 = \boldsymbol{u}_{m-1}^0 + \boldsymbol{H}^{\mathrm{SI}}(\boldsymbol{u}_{m-1}^0, \boldsymbol{u}_{m-1}^0, \boldsymbol{u}_m^0, \Delta t_m)\,, \quad m = 1, \dots M, \tag{18}$$

and the two-stage predictor SI(2)

$$\begin{aligned} \boldsymbol{u}^{(1)} &= \boldsymbol{u}_{m-1}^0 + \boldsymbol{H}^{\mathrm{SI}}(\boldsymbol{u}_{m-1}^0, \boldsymbol{u}_{m-1}^0, \boldsymbol{u}^{(1)}, \Delta t_m)\,, \quad m = 1, \dots M, \\ \boldsymbol{u}_m^0 &= \boldsymbol{u}_{m-1}^0 + \boldsymbol{H}^{\mathrm{SI}}(\boldsymbol{u}^{(1)}, \boldsymbol{u}_{m-1}^0, \boldsymbol{u}_m^0, \Delta t_m)\,, \quad m = 1, \dots M\,, \end{aligned} \tag{19}$$

where

$$\boldsymbol{H}^{\mathrm{SI}}(\boldsymbol{u}_a, \boldsymbol{u}_b, \boldsymbol{u}_c, \Delta t_m) = \Delta t_m \left[-\partial_x \boldsymbol{f}_{\mathrm{c}}(\boldsymbol{u}_a) + \partial_x \left(\frac{\Delta t_m}{2} \boldsymbol{A}_{\mathrm{c}}(\boldsymbol{u}_b)^2 + \boldsymbol{A}_{\mathrm{d}}(\boldsymbol{u}_b)\right) \partial_x \boldsymbol{u}_c\right]. \tag{20}$$

These correctors are motivated by the implicit Lax-Wendroff method and have excellent stability properties [44]. The corrector equation of the SDC method to calculate the k-th approximation is given by

$$\boldsymbol{u}_m^k = \boldsymbol{u}_{m-1}^k + \Delta t \sum_{i=1}^{M} w_{m,i}^{\mathrm{NN}} \boldsymbol{f}(\boldsymbol{u}_i^{k-1}, t_i) + \Delta \boldsymbol{H}_m^k\,, \quad m = 1, \dots M. \tag{21}$$

The deltas of the low-order terms $\boldsymbol{H}_m^k$ for the different time integrations schemes are defined as follows. Firstly, the IMEX Euler:

$$\Delta \boldsymbol{H}_m^{k,\mathrm{EU}} = \boldsymbol{H}^{\mathrm{EU}}(\boldsymbol{u}_{m-1}^k, \boldsymbol{u}_m^k, \Delta t_m) - \boldsymbol{H}^{\mathrm{EU}}(\boldsymbol{u}_{m-1}^{k-1}, \boldsymbol{u}_m^{k-1}, \Delta t_m). \tag{22}$$

The SI(1) and SI(2) deltas are

$$\Delta \boldsymbol{H}_m^{k,\mathrm{SI}(1)} = \boldsymbol{H}^{\mathrm{SI}}(\boldsymbol{u}_{m-1}^k, \boldsymbol{u}_{m-1}^k, \boldsymbol{u}_m^k, \Delta t_m) - \boldsymbol{H}^{\mathrm{SI}}(\boldsymbol{u}_{m-1}^{k-1}, \boldsymbol{u}_{m-1}^{k-1}, \boldsymbol{u}_m^{k-1}, \Delta t_m) \tag{23}$$

and, respectively,

$$\Delta \boldsymbol{H}_m^{k,\mathrm{SI}(2)} = \boldsymbol{H}^{\mathrm{SI}}(\boldsymbol{u}^{(1)}, \boldsymbol{u}_{m-1}^{k}, \boldsymbol{u}_m^{k}, \Delta t_m) - \boldsymbol{H}^{\mathrm{SI}}(\boldsymbol{u}_m^{k-1}, \boldsymbol{u}_{m-1}^{k-1}, \boldsymbol{u}_m^{k-1}, \Delta t_m) \tag{24}$$

with

$$\begin{aligned} \boldsymbol{u}^{(1)} &= \boldsymbol{u}_{m-1}^{k} + \Delta t \sum_{i=1}^{M} w_{m,i}^{\mathrm{NN}} \boldsymbol{f}(\boldsymbol{u}_i^{k-1}, t_i) \\ &\quad + \boldsymbol{H}^{\mathrm{SI}}(\boldsymbol{u}_{m-1}^{k}, \boldsymbol{u}_{m-1}^{k}, \boldsymbol{u}^{(1)}, \Delta t_m) - \boldsymbol{H}^{\mathrm{SI}}(\boldsymbol{u}_{m-1}^{k-1}, \boldsymbol{u}_{m-1}^{k-1}, \boldsymbol{u}_m^{k-1}, \Delta t_m), \quad m = 1, \dots M. \end{aligned} \tag{25}$$

Remark 2. *Implementation note: In practice, the $\boldsymbol{H}$ terms from sweep $k-1$ are stored to ensure efficient computation in subsequent sweeps.*

For readability, the EU, $\mathrm{SI}(1)$, or $\mathrm{SI}(2)$ superscripts are omitted in the following discussion, as the SDC formulation remains identical across these time integration schemes. Upon convergence $\Delta \boldsymbol{H}_m^k \to \boldsymbol{0}$ and the incremental CM (12) is recovered. Selecting Radau Right points for the collocation leads to the Radau IIA method resulting in a convergence of order $2M-1$ (see [12, Ch. 6]) while selecting Lobatto points leads to the Lobatto IIIA method of order $2M-2$ (see [12, Ch. 8]). The residual of the incremental SDC method for the k-th approximation reads

$$\boldsymbol{r}_m^k = \boldsymbol{u}_m^k - \boldsymbol{u}_{m-1}^k - \Delta t \sum_{i=1}^{M} w_{m,i}^{\mathrm{NN}} \boldsymbol{f}(\boldsymbol{u}_i^{k-1}, t_i), \quad m = 1, \dots M. \tag{26}$$

3.4. Non-incremental collocation method. Until now, the method discussed has swept through the subintervals from node to node. There exists an equivalent formulation, called *zero-to-node* or non-incremental formulation, for which the collocation method reads

$$\boldsymbol{u}_m = \boldsymbol{u}_0 + \Delta t \sum_{i=1}^{M} w_{m,i}^{\mathrm{0N}} \boldsymbol{f}(\boldsymbol{u}_i, t_i), \quad m = 1, \dots M, \tag{27}$$

where zero-to-node weights are given by

$$w_{m,i}^{\mathrm{0N}} = \sum_{j=1}^{m} w_{j,i}^{\mathrm{NN}}. \tag{28}$$

This form resembles the standard form of the CM and can be achieved by recursive substitution of $\boldsymbol{u}_{m-1}$ in (12). As a system, the non-incremental CM reads

$$\underline{\boldsymbol{F}}^{\mathrm{0N}}(\underline{\boldsymbol{u}}) = \underline{\boldsymbol{0}}. \tag{29}$$

Remark 3. *In collocation methods, the coefficients are denoted a_{ij} as, for example, in [20, Ch. 2]. Here, the notation $w_{m,i}^{\mathrm{0N}}$ similar to the incremental method is chosen for better comparison.*

3.5. Non-incremental SDC method. Similarly, one obtains the non-incremental SDC method

$$\boldsymbol{u}_m^k = \boldsymbol{u}_0 + \Delta t \sum_{i=1}^{M} w_{m,i}^{\mathrm{0N}} \boldsymbol{f}(\boldsymbol{u}_i^{k-1}, t_i) + \sum_{i=1}^{m} \Delta \boldsymbol{H}_i^k, \quad m = 1, \dots M. \tag{30}$$

Note that the correction terms in (30) are composed of the same deltas as in the incremental form, but are summed up over the current and all preceding subintervals. The convergence of the zero-to-node SDC method recovers the non-incremental collocation method (27).

Remark 4. *SDC can also be interpreted as a preconditioned Picard iteration for the collocation problem, see e.g. [1], [41], [46].*

4. Multilevel collocation and SDC methods

All multilevel techniques derived and applied in this section originate from Brandt [6] and can be comprehended there in great detail. Firstly, a sequence of grid levels l, from a coarse discretization of the computational domain ($l = 1$) to a fine discretization ($l = L$) is considered. The variable $\underline{\boldsymbol{u}}$ denotes from now on the solution on all levels. The basic idea is to utilize a coarser grid solution to accelerate convergence on a finer grid or, conversely, to leverage the finer grid to improve the solution on the coarser grid. These objectives are achieved with the Full Approximation Scheme (FAS). With FAS there is ideally a fully-fledged solution to the fine grid problem at all levels.

4.1. Incremental multilevel collocation. The nodal solution vector on level $l = 1, \dots, L$ is denoted by $\underline{\boldsymbol{u}}_l = \left[\{\boldsymbol{u}_{l,m}\}_{m=1}^{M_l}\right]$. The FAS-ML (Full Approximation Scheme Multi-Level) framework is designed to approximate solutions across multiple levels. The representation on level l is given by

$$\underline{\boldsymbol{F}}_l^{\mathrm{NN}}(\tilde{\underline{\boldsymbol{u}}}_l) = \underline{\boldsymbol{g}}_l^{\mathrm{NN}}(\tilde{\underline{\boldsymbol{u}}}_{l+1})\,., \quad l = 1, \dots, L \tag{31}$$

The primary distinction between the single-level and multilevel case is the introduction of the FAS right-hand side (RHS), $\underline{\boldsymbol{g}}_l^{\mathrm{NN}}$. This addition ensures that all levels collectively approximate the solution on the finest grid. The FAS RHS is defined by

$$\underline{\boldsymbol{g}}_l^{\mathrm{NN}}(\tilde{\underline{\boldsymbol{u}}}_{l+1}) = \begin{cases} \underline{\boldsymbol{F}}_l^{\mathrm{NN}}(\underline{\mathcal{P}}_l \tilde{\underline{\boldsymbol{u}}}_{l+1}) + \underline{\mathcal{R}}_l\left(\underline{\boldsymbol{g}}_{l+1}^{\mathrm{NN}} - \underline{\boldsymbol{F}}_{l+1}^{\mathrm{NN}}(\tilde{\underline{\boldsymbol{u}}}_{l+1})\right) & l < L \\ 0 & l = L \end{cases} \tag{32}$$

Here, $\tilde{\underline{\boldsymbol{u}}}_{l+1}$ denotes an approximate solution on level $l+1$ after one or more SDC sweeps. The term $\underline{\boldsymbol{g}}_l^{\mathrm{NN}}(\tilde{\underline{\boldsymbol{u}}}_{l+1})$ is computed prior to the correction sweep at the start of every multigrid cycle and contains information from the finer grids, detailed further in algorithm 2. Transfer operators are introduced to facilitate interactions between different levels. To transfer residuals to the next coarser level, we use the residual restriction $\underline{\boldsymbol{r}}_l = \underline{\mathcal{R}}_l \underline{\boldsymbol{r}}_{l+1}$. Similarly, the solution projection to the next coarser level is represented by $\underline{\boldsymbol{v}}_l = \underline{\mathcal{P}}_l \underline{\boldsymbol{u}}_{l+1}$, and the solution interpolation to the next finer level is given by $\underline{\boldsymbol{u}}_l = \underline{\mathcal{I}}_l \underline{\boldsymbol{u}}_{l-1}$.

Remark 5. *The transfer operators are algebraic matrices and are applied to the coefficient vectors.*

Convergence within the FAS-ML framework is characterized by several key behaviors. In addition to the convergence of the solution $\tilde{\underline{\boldsymbol{u}}}_l \to \underline{\boldsymbol{u}}_l$ at each level, the residual for levels $l < L$ converge $\underline{\boldsymbol{r}}_l^{\mathrm{NN}} = \underline{\boldsymbol{g}}_l^{\mathrm{NN}} - \underline{\boldsymbol{F}}_{l+1}^{\mathrm{NN}}(\tilde{\underline{\boldsymbol{u}}}_l) \to \underline{\boldsymbol{0}}$. Concurrently, the right-hand side (RHS) $\underline{\boldsymbol{g}}_l^{\mathrm{NN}}$ for $l < L$ trends towards $\underline{\boldsymbol{F}}_l^{\mathrm{NN}}(\underline{\mathcal{P}}_l \underline{\boldsymbol{u}}_{l+1})$, emphasizing the alignment of the RHS computation with the projected solutions from higher levels. These properties result in the formulation of the incremental multilevel collocation method, defined by the equations:

$$\underline{\boldsymbol{F}}_l^{\mathrm{NN}}(\underline{\boldsymbol{u}}_l) \;= \underline{\boldsymbol{F}}_l^{\mathrm{NN}}(\underline{\mathcal{P}}_l \underline{\boldsymbol{u}}_{l+1})\,, \quad l = 1, \dots L-1, \tag{33a}$$

$$\underline{\boldsymbol{F}}_L^{\mathrm{NN}}(\underline{\boldsymbol{u}}_L) = \underline{\boldsymbol{0}}. \tag{33b}$$

4.2. MLSDC transfer operators. The solution is interpolated from level $l-1$ to level l using the interpolation operator

$$\underline{\boldsymbol{u}}_l = \underline{\mathcal{I}}_l \underline{\boldsymbol{u}}_{l-1}. \tag{34}$$

This operator relies on embedded interpolation techniques, where the operator $\underline{\mathcal{I}}_l$ transfers the coarse solution accurately to the fine grid with no other than round-off errors. Similarly, the solution can be projected from level l to $l-1$ using the projection operator

$$\underline{\boldsymbol{v}}_l = \underline{\mathcal{P}}_l \underline{\boldsymbol{u}}_{l+1}\,, \tag{35}$$

for which there is a choice between L^2-projection and embedded interpolation. While L^2-projection is conservative, it is less accurate than embedded interpolation as it relies on the lower level basis functions. In this paper, both methods for projection are implemented and investigated later on. The residual restriction operator $\underline{\mathcal{R}}_l$ from level l to $l-1$ is defined as the transpose of the interpolation operator:

$$\underline{\mathcal{R}}_l \underline{\boldsymbol{r}}_{l+1} = \underline{\mathcal{I}}_{l+1}^{\mathrm{t}} \underline{\boldsymbol{r}}_{l+1}. \tag{36}$$

4.3. Incremental multilevel SDC method. Similarly to SDC, the multilevel SDC method is formulated as an iterative solver to the collocation method.The corrector equations on level l are given by

$$\boldsymbol{u}_{l,m}^k = \boldsymbol{u}_{l,m-1}^k + \Delta t \sum_{i=1}^{M_l} w_{l,mi}^{\mathrm{NN}} \boldsymbol{f}(\boldsymbol{u}_{l,i}^{k-1}, t_{l,i}) + \boldsymbol{g}_{l,m}^{\mathrm{NN}} + \Delta \boldsymbol{H}_{l,m}^k, \quad m = 1, \dots M_l. \tag{37}$$

The definitions of $\Delta \boldsymbol{H}_{l,m}^k$ for the three different time integrators are given in equations (22) to (24).

Remark 6. *The k-th iteration $\underline{\boldsymbol{u}}_l^k$ is always an approximation to the discrete solution $\underline{\boldsymbol{u}}_l$ and therefore one specific $\underline{\tilde{\boldsymbol{u}}}_l$. The tilde $\underline{\tilde{\boldsymbol{u}}}_l$ indicator is left out in favor of readability.*

To express the MLSDC correction scheme in a compact form, its matrix form is introduced:

$$\underline{\boldsymbol{F}}_l^{\mathrm{NN}}(\underline{\boldsymbol{u}}_l^k) = \underline{\boldsymbol{g}}_l^{\mathrm{NN}} + \underline{\boldsymbol{C}}_l^{\mathrm{NN}} \Delta \underline{\boldsymbol{H}}_l^k, \tag{38}$$

where $\underline{\boldsymbol{C}}_l^{\mathrm{NN}}$ is identity matrix and can be omited

$$\underline{\boldsymbol{C}}_l = \begin{bmatrix} 1 & 0 & \cdots & 0 \\ 0 & \ddots & & \vdots \\ \vdots & & \ddots & 0 \\ 0 & \cdots & 0 & 1 \end{bmatrix}. \tag{39}$$

Upon convergence $\Delta \underline{\boldsymbol{H}}_l^k \to \underline{\boldsymbol{0}}$ and the incremental multilevel CM is recovered. The procedure for an incremental MLSDC correction sweep can be seen in algorithm 1, the index l dropped for readability.

Algorithm 1 Incremental MLSDC correction sweeps.

procedure MLSDC_Corrector($\underline{\boldsymbol{u}}, \underline{\boldsymbol{g}}, N$)
  $\underline{\boldsymbol{u}}^0 \leftarrow \underline{\boldsymbol{u}}$
  for $k = 1, N$ **do**
    $\boldsymbol{u}_0^k \leftarrow \boldsymbol{u}_0$
    for $m = 1, M$ **do**
      $\boldsymbol{u}_m^k \leftarrow \mathrm{Solve}\left(\boldsymbol{u}_m^k = \boldsymbol{u}_{m-1}^k + \Delta t \sum_{i=1}^{M} w_{m,i}^{\mathrm{NN}} \boldsymbol{f}(\boldsymbol{u}_i^{k-1}, t_i) + \Delta \boldsymbol{H}_m^k + g_m^{\mathrm{NN}}\right)$
    end for
  end for
  $\underline{\boldsymbol{u}} \leftarrow \underline{\boldsymbol{u}}^N$
end procedure

The incremental MLSDC residual reads

$$\underline{\boldsymbol{r}}_l^{\mathrm{NN}} = \underline{\boldsymbol{g}}_l^{\mathrm{NN}} - \underline{\boldsymbol{F}}_l^{\mathrm{NN}}(\underline{\boldsymbol{u}}_l). \tag{40}$$

4.4. Non-incremental multilevel collocation. An analogous procedure to the non-incremental CM method yields the non-incremental multilevel collocation method, which is defined by the equations:

$$\underline{\boldsymbol{F}}_l^{0\mathrm{N}}(\underline{\tilde{\boldsymbol{u}}}_l) = \underline{\boldsymbol{F}}_l^{0\mathrm{N}}(\underline{\mathcal{P}}_l \underline{\boldsymbol{u}}_{l+1}), \quad l = 1, \dots L-1, \tag{41a}$$

$$\underline{\boldsymbol{F}}_L^{0\mathrm{N}}(\underline{\tilde{\boldsymbol{u}}}_L) = \underline{\mathbf{0}}. \tag{41b}$$

4.5. Non-incremental multilevel SDC method. The matrix form of the non-incremental MLSDC method reads

$$\underline{\boldsymbol{F}}_l^{0\mathrm{N}}(\underline{\boldsymbol{u}}_l^k) = \underline{\boldsymbol{g}}_l^{0\mathrm{N}} + \underline{\boldsymbol{C}}_l^{0\mathrm{N}} \Delta \underline{\boldsymbol{H}}_l^k, \tag{42}$$

with

$$\underline{\boldsymbol{C}}_l^{0\mathrm{N}} = \begin{bmatrix} 1 & 0 & \cdots & 0 \\ 1 & 1 & \cdots & 0 \\ \vdots & \vdots & \ddots & \vdots \\ 1 & 1 & \cdots & 1 \end{bmatrix}. \tag{43}$$

Again the non-incremental multilevel collocation method is recovered upon convergence.

4.6. Non-equivalence of incremental and non-incremental multilevel-methods. Equivalence is obvious for multilevel collocation, but not for multilevel SDC. For single-level CM and SDC, the incremental and non-incremental formulations are equivalent via recursion, but for MLSDC equivalence requires

$$\underline{\boldsymbol{g}}_l^{0\mathrm{N}} = \underline{\boldsymbol{C}}_l^{0\mathrm{N}}\, \underline{\boldsymbol{g}}_l^{\mathrm{NN}}. \tag{44}$$

For a two-level case the condition (44) can be demonstrated. An illustrative example is provided in Appendix A. Substituting the definition of the RHS and exploiting $\underline{\boldsymbol{F}}_l^{0\mathrm{N}} = \underline{\boldsymbol{C}}_l^{0\mathrm{N}} \underline{\boldsymbol{F}}_l^{\mathrm{NN}}$ yields

$$\underline{\mathcal{R}}_l \big(\underline{\boldsymbol{g}}_{l+1}^{0\mathrm{N}} - \underline{\boldsymbol{F}}_{l+1}^{0\mathrm{N}}(\underline{\boldsymbol{u}}_{l+1}^k) \big) = \underline{\boldsymbol{C}}_l^{0\mathrm{N}}\, \underline{\mathcal{R}}_l \big(\underline{\boldsymbol{g}}_{l+1}^{\mathrm{NN}} - \underline{\boldsymbol{F}}_{l+1}^{\mathrm{NN}}(\underline{\boldsymbol{u}}_{l+1}^k) \big). \tag{45}$$

For $l = L-1$ we have $\underline{\boldsymbol{g}}_{l+1}^{\mathrm{NN}} = \underline{\boldsymbol{g}}_{l+1}^{0\mathrm{N}} = \underline{\mathbf{0}}$, which implies

$$\underline{\mathcal{R}}_{L-1} \underline{\boldsymbol{F}}_L^{0\mathrm{N}}(\underline{\boldsymbol{u}}_L^k) = \underline{\boldsymbol{C}}_{L-1}^{0\mathrm{N}}\, \underline{\mathcal{R}}_{L-1} \underline{\boldsymbol{F}}_L^{\mathrm{NN}}(\underline{\boldsymbol{u}}_L^k), \tag{46}$$

or equivalently

$$\underline{\mathcal{R}}_{L-1} \underline{\boldsymbol{C}}_L^{0\mathrm{N}} \underline{\boldsymbol{F}}_L^{\mathrm{NN}}(\underline{\boldsymbol{u}}_L^k) = \underline{\boldsymbol{C}}_{L-1}^{0\mathrm{N}}\, \underline{\mathcal{R}}_{L-1} \underline{\boldsymbol{F}}_L^{\mathrm{NN}}(\underline{\boldsymbol{u}}_L^k). \tag{47}$$

As the construction of the transfer operators is independent of the mesh level it follows that

$$\underline{\mathcal{R}}_l \underline{\boldsymbol{C}}_{l+1}^{0\mathrm{N}} = \underline{\boldsymbol{C}}_l^{0\mathrm{N}} \underline{\mathcal{R}}_l \tag{48}$$

is a necessary condition for the equivalence of incremental and non-incremental MLSDC. The above condition is not universally satisfied and can be refuted by a numerical example. Consider $L = 2$ with $M_2 = 3$, $M_1 = 2$ and Radau Right points with p coarsening in time. The operators for both cases result in:

$$\underline{\boldsymbol{C}}_l^{0\mathrm{N}} \underline{\mathcal{R}}_l = \begin{bmatrix} 1.22499 & 0.33594 & -0.07321 & 0.00000 \\ 0.87674 & 1.19970 & 0.69907 & 0.00000 \\ 1.00000 & 1.00000 & 1.00000 & 1.00000 \end{bmatrix}$$

and

$$\underline{\mathcal{R}}_l \underline{\boldsymbol{C}}_{l+1}^{0\mathrm{N}} = \begin{bmatrix} 1.48773 & 0.26274 & -0.07321 & 0.00000 \\ 1.28778 & 1.63603 & 0.77227 & 0.00000 \\ 1.22449 & 1.10123 & 1.30093 & 1.00000 \end{bmatrix}$$

Proposition 1. *The incremental and non-incremental MLSDC formulations are not equivalent.*

The outcome is similar for Lobatto and equidistant collocation points, which shows that incremental and non-incremental MLSDC are not equivalent, although they converge to the same solution.

4.7. Multilevel algorithm. In this subsection, we provide a detailed explanation of the MLSDC framework, which consists of a starting strategy combined with a V-Cycle. The algorithms for the V-cycle (algorithm 2) and the various strategies for initiating an MLSDC algorithm (algorithms 3 and 4) are presented below. All of them are formally identical for incremental and non-incremental MLSDC, so the NN and 0N indices are dropped. The V-cycle is started at the fine level $l = L$ with

Algorithm 2 MLSDC V-cycle.

1: **procedure** Incremental MLSDC_V_Cycle($\underline{\boldsymbol{u}}, N_c, L$)
2: $\quad \underline{\boldsymbol{g}}_L \leftarrow \underline{\mathbf{0}}$
3: $\quad$ **for** $l = L, 2, -1$ **do**
4: $\quad\quad$ SDC_Corrector($\underline{\boldsymbol{u}}_l, \underline{\boldsymbol{g}}_l, N_s = 1$) ▷ Pre-sweeping
5: $\quad\quad \underline{\boldsymbol{r}}_l \leftarrow \underline{\boldsymbol{g}}_l - \underline{\boldsymbol{F}}_l(\underline{\boldsymbol{u}}_l)$ ▷ Residual evaluation
6: $\quad\quad \underline{\boldsymbol{v}}_{l-1} \leftarrow \underline{\mathcal{P}}_{l-1}\underline{\boldsymbol{u}}_l$ ▷ Solution restriction
7: $\quad\quad \underline{\boldsymbol{g}}_{l-1} \leftarrow \underline{\boldsymbol{F}}_{l-1}(\underline{\boldsymbol{v}}_{l-1}) + \underline{\mathcal{R}}_{l-1}\underline{\boldsymbol{r}}_l$ ▷ RHS composition
8: $\quad$ **end for**
9: $\quad$ SDC_Corrector($\underline{\boldsymbol{u}}_1, \underline{\boldsymbol{g}}_1, N_c$) ▷ Coarse solution
10: $\quad$ **for** $l = 2, L$ **do**
11: $\quad\quad \underline{\boldsymbol{u}}_l \leftarrow \underline{\boldsymbol{u}}_l + \underline{\mathcal{I}}_l(\underline{\boldsymbol{u}}_{l-1} - \underline{\boldsymbol{v}}_{l-1})$ ▷ Correction prolongation
12: $\quad\quad$ **if** $l < L$ **then**
13: $\quad\quad\quad$ SDC_Corrector($\underline{\boldsymbol{u}}_l, \underline{\boldsymbol{g}}_l, N_s = 1$) ▷ Post-sweeping
14: $\quad\quad$ **end if**
15: $\quad$ **end for**
16: **end procedure**

a SDC sweep. Pre-sweeping is used to eliminate high-frequency error components on the finer grid, while low-frequency errors are removed on the coarse grid. Then the solution and residuals are restricted to the coarser grids with the operators described in 4.2. The FAS right-hand side $\underline{\boldsymbol{g}}_l$ is subsequently calculated with equation (32). At the bottom level $l = 1$, the problem is solved using N_c coarse sweeps. Finally, the correction is interpolated to the finer grids (line 11 in algorithm 2). This correction is the key for boosting convergence. A post-sweeping step is performed for levels $1 < l < L$, after that the cycle starts again with the current solution. Only on the last cycle a post-sweeping SDC sweep is optionally performed on the finest grid. The number of post- and pre-sweeping steps N_s could differ from 1, conducted numerical studies do not suggest any benefit from that, so all tests were simply done with $N_s = 1$ sweep for pre- and post-sweeping.
Initial solutions on every grid are required with FAS. Therefore, certain starting strategies to produce $\underline{\boldsymbol{u}}_L^0$ are needed. One strategy is to spread the initial conditions as a constant through all nodes [42]. The second strategy investigated in the present work is to start with the predictor solutions on all levels. The third strategy, referred to as the Cascade (algorithm 3) [23] begins with a predictor on the coarse grid, followed by a single correction sweep. The solution is then interpolated onto the next finer grid, where another correction is performed. On the finest grid, the V-cycle starts with the pre-sweeping step for the interpolated solution from the second finest grid. The fourth and final approach is utilizing MLSDC as a Full Multigrid (FMG) method, as outlined in algorithm 4 (compare FMG in [6, Fig. 1.2]).The algorithm 4 shows the FMG_{n_C} starting variant with

Algorithm 3 MLSDC Cascade.

procedure MLSDC_Cascade($\underline{\boldsymbol{u}}, L$)
  SDC_Predictor($\underline{\boldsymbol{u}}_1$) ▷ Predictor Solution Level 1
  for $l = 1, L-1$ **do**
    SDC_Corrector($\underline{\boldsymbol{u}}_l, \underline{\boldsymbol{g}}_l = \underline{\mathbf{0}}, N_s = 1$) ▷ Corrector Sweep
    $\underline{\boldsymbol{u}}_{l+1} \leftarrow \underline{\mathcal{I}}_{l+1}(\underline{\boldsymbol{u}}_l)$ ▷ Solution interpolation
  end for
end procedure

the number of cycles $n_C = 1$ per added level. Rather than improving the initial solution with a corrector sweep, as done in the Cascade variant, we substitute the corrector with one or more V-Cycles on a growing subset of levels. To ensure that each level converges to its solution before moving to the next, there is the possibility to perform multiple V-cycles per added level, contrary to just one per level like in [6]). Note that for 2 levels, the starting strategies from algorithm 3 and 4 are identical.

Algorithm 4 MLSDC FMG$_{n_C}$.

procedure MLSDC_FMG$_{n_C}$($\underline{\boldsymbol{u}}, N_c, L, n_C$)
  SDC_Predictor($\underline{\boldsymbol{u}}_1$) ▷ Predictor Solution Level 1
  SDC_Corrector($\underline{\boldsymbol{u}}_1, \underline{\boldsymbol{g}}_1 = \underline{\mathbf{0}}, N_s = 1$) ▷ Corrector Sweep Level 1
  $\underline{\boldsymbol{u}}_2 \leftarrow \underline{\mathcal{I}}_2(\underline{\boldsymbol{u}}_1)$ ▷ Solution interpolation
  for $l = 2, L-1$ **do**
    for $c = 1, n_C$ **do**
      MLSDC_V-cycle($\underline{\boldsymbol{u}}, N_c, l$) ▷ n_C MLSDC V-cycles
    end for
    $\underline{\boldsymbol{u}}_{l+1} \leftarrow \underline{\mathcal{I}}_{l+1}(\underline{\boldsymbol{u}}_l)$ ▷ Solution interpolation
  end for
end procedure

For illustration, the cascadic and FMG strategies are sketched in Figure 1. The coarse level, corresponding to $l = 1$, is located at the bottom of the sketch. Both strategies begin with the coarse solution at the bottom left, the notation $\mathcal{R} + \mathcal{P}$ represents fine-to-coarse operations (restriction and projection), while $\mathcal{I}\Delta u$ denotes coarse-to-fine prolongation of the correction. The different markers indicate specific operations: a single circle represents a corrector step, whereas two circles correspond to a predictor-corrector sequence. This notation is not applied within the V-cycles, where SDC sweeps also take place. The first V-Cycle after the start is highlighted in blue.

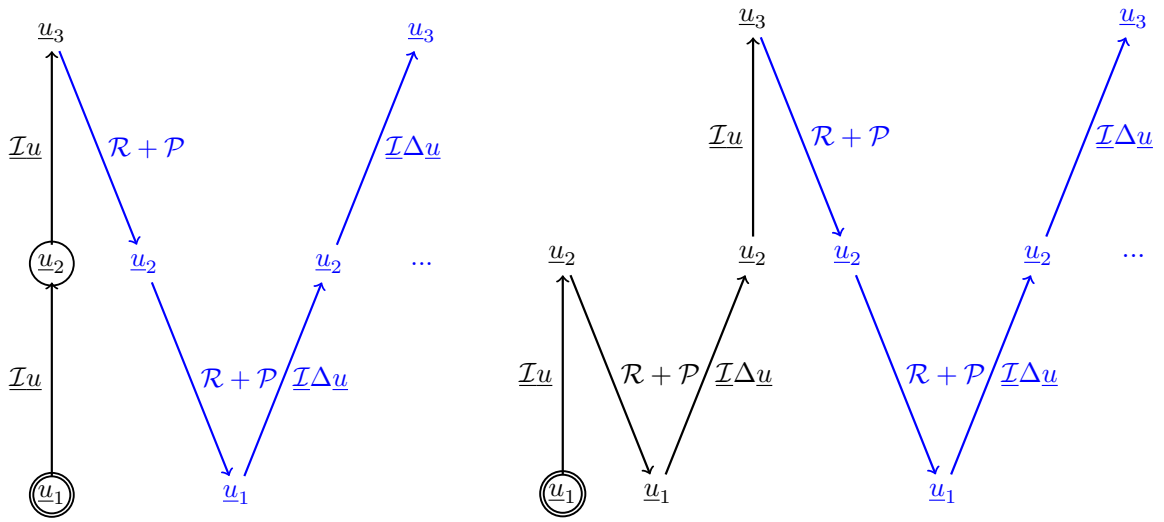

(a) Cascadic starting strategy

(b) FMG_1 starting strategy

Figure 1. Sketches for the starting strategies Cascade and FMG_1 with one attached V-cycle

5. Temporal stability and accuracy

In this section, the stability and accuracy properties of the MLSDC method are investigated. Starting point for the stability analysis is the convection-diffusion equation (5) with a spatially periodic complex solution $u(x,t) = \hat{u}(t)\mathrm{e}^{\mathrm{i}kx}$ and a constant velocity $v \in \mathbb{R}$, which yields

$$\partial_t \hat{u}\mathrm{e}^{\mathrm{i}kx} = -\partial_x(v\hat{u}\mathrm{e}^{\mathrm{i}kx}) + \partial_x(\nu\partial_x\hat{u}\mathrm{e}^{\mathrm{i}kx}). \tag{49}$$

With the definitions from Section 2, we note that

$$\begin{aligned} f_c &= v\hat{u}(t)\mathrm{e}^{\mathrm{i}kx} = \hat{f}_c(t)\mathrm{e}^{\mathrm{i}kx}, \\ f_d &= \nu\partial_x\hat{u}(t)\mathrm{e}^{\mathrm{i}kx} = \hat{f}_d(t)\mathrm{e}^{\mathrm{i}kx}. \end{aligned} \tag{50}$$

It follows that $A_c = \hat{A}_c = v$ and $A_d = \hat{A}_d = \nu$. This can now simply be plugged into the predictor and corrector equations shown in Section 3 and Section 4. If the spatial derivatives are evaluated, $\mathrm{e}^{\mathrm{i}kx}$ can be cancelled out and a Dahlquist-type ODE [11] in time is obtained,

$$\mathrm{d}_t\hat{u} = \lambda\hat{u}. \tag{51}$$

Here $\lambda \in \mathbb{C}$ with the real part $\lambda_\mathrm{r} = -\nu k^2$ and the imaginary part $\lambda_\mathrm{i} = -vk$.

Remark 7. *Although the MLSDC methods were developed for PDEs with a real solution $u(x,t)$, they can be easily adopted for the present problem. After removing the common factor $\mathrm{e}^{\mathrm{i}kx}$, the complex amplitudes $\hat{H}_m^k$, $\Delta\hat{H}_m^k$ and $\hat{f}(\hat{u}_i, t_i)$ take the role of H_m^k, ΔH_m^k and $\hat{f}(u_i, t_i)$ respectively.*

5.1. Stability. The stability function can be obtained by computing the ratio of the amplitudes of two subsequent time steps, i.e.,

$$R(z) = \frac{\hat{u}^{n+1}}{\hat{u}^n}, \tag{52}$$

where $z = \Delta t \lambda$. The set $\{z \in \mathbb{C}; |R(z)| \leq 1\}$ is the stability domain of the method. The method is called A-stable if $|R(z)| \leq 1$ for all z with $z_i \leq 0$ and L-stable if, in addition, $R = 0$ for $z \to \infty$.

Remark 8. *For conservation laws, $|z_i| = \Delta t |v| k$ can be associated with the CFL number and $-z_r = \Delta t \nu k^2$ with the diffusion number of the fully discrete problem.*

The stability of the correctors and predictors for IMEX Euler, SI(1) and SI(2) discussed in Section 4 was investigated. SI(a,b) means SI(a) used for the predictor and SI(b) for the corrector. It is to be noted, that the predictor will also be used for the FMG starting strategy. For the tests, one time step is performed with $\Delta t = 1$ and an initial condition $\hat{u}(0) = 1$. Figure 2 shows representative neutral stability curves for MLSDC with the predictor and FMG_1 starting strategy using 3 levels with $M_l = (3, 5, 7)$. Radau Right collocation points were used and C cycles performed. For example, MLSDC-SI(2,2)$^{C+1}_{3,5,7}$ means a MLSDC method with the SI(2) time integrator as a predictor and corrector, with 3 levels and a number of fine grid iterations $N = C + 1$. This notation shall help with the comparability to single-level SDC methods. The number of coarse sweeps was set to $N_c = 2$.
Intuitively, one would only look at stability curves on the finest grid, but through FAS there are full solutions on all grids, which interact via the right-hand side. One apprehension may therefore be that instabilities of the coarsest discretization will propagate to the fine grid. An initial observation reveals that the stability of the multilevel SDC is slightly inferior to that of the single-level SDC [44], but the difference is marginal, and the multilevel method still performs remarkably well overall. For a comparison to the single-level SDC methods, refer to Appendix B. It is further noticed, that the stability properties are rather similar on all levels, compare Figure 2a with Figure 2b. When comparing the SI(1) and SI(2) correctors to the single-level stability curves for $M = 3$ (Appendix B, Figure 16), the stability doesn't seem to be dictated by the stability of the coarsest level. Compared to IMEX Euler, SI(1,1) yields a clear improvement in stability, which is further enhanced by the two-stage method SI(2,2). The stability of the IMEX Euler method cannot keep up with the new SI time integrators and will no longer be considered from now on. The predictor and FMG_1 starting variants hardly differ in stability with the predictor variant being slightly more stable possibly due to the interpolation within the FMG start, compare Figure 2c and 2e or 2d and 2f. Increasing the number of cycles slowly erodes the stability, which complies with [44]. A possible explanation may be given by the gradual removal of the artificial diffusion of SI(1) and SI(2) in both, single-level and multilevel SDC methods. This proceeds more rapidly for MLSDC, which may be the reason why the latter fails to preserve the L-stability of the related single-level method. A test with optimal SDC variants for each level, as identified in [44, Table 1], does not improve the stability here.

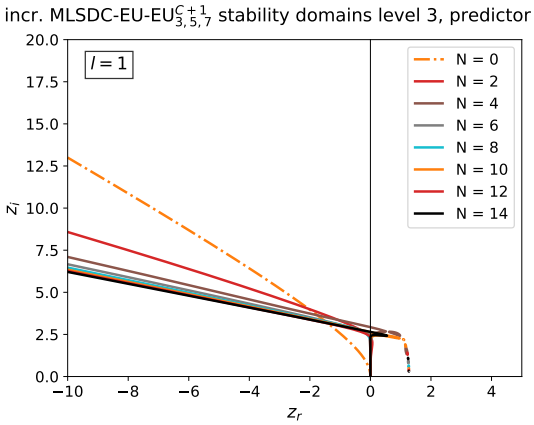

(a) Bottom level $l = 1$ of MLSDC with IMEX Euler on all levels, predictor variant

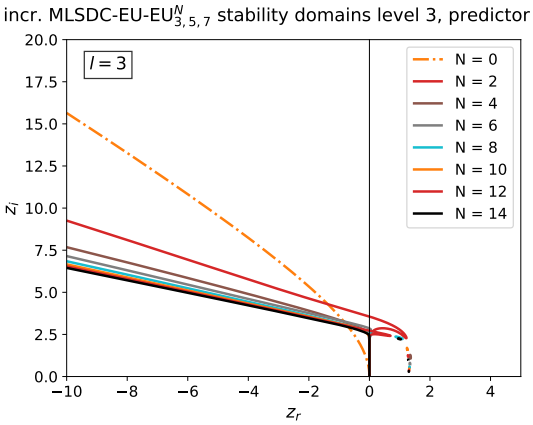

(b) Top level $l = 3$ of MLSDC with IMEX Euler on all levels, predictor variant

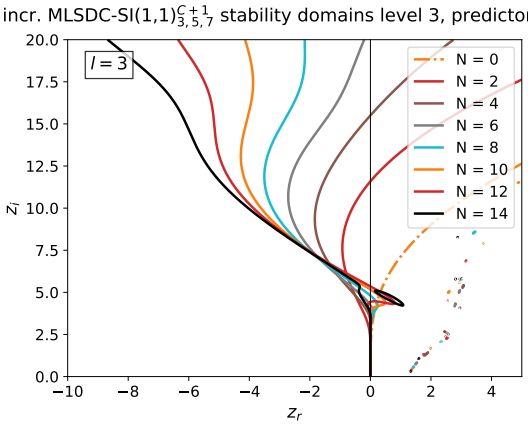

(c) Top level $l = 3$ of MLSDC with SI(1) on all levels, predictor variant

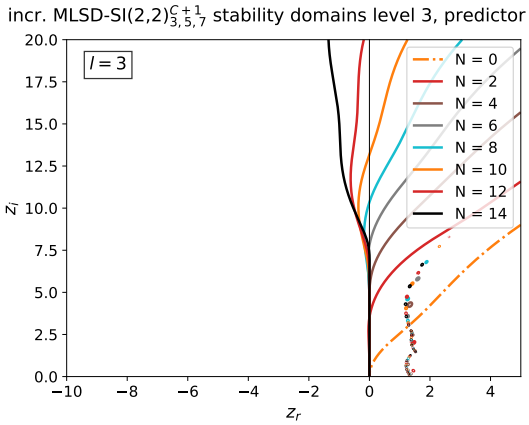

(d) Top level $l = 3$ of MLSDC with SI(2) on all levels, predictor variant

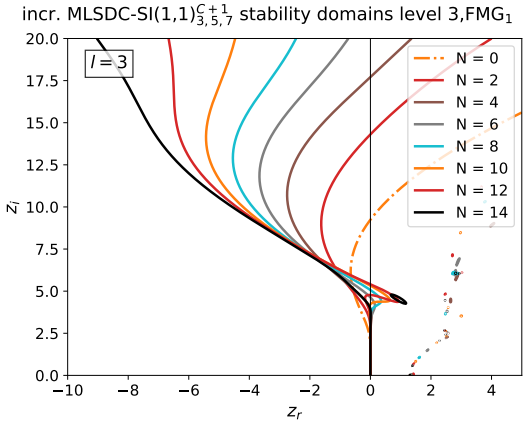

(e) Top level $l = 3$ of MLSDC with SI(1) on all levels, FMG$_1$ variant

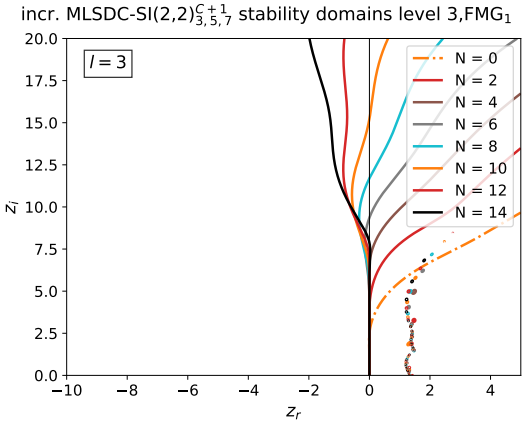

(f) Top level $l = 3$ of MLSDC with SI(2) on all levels, FMG$_1$ variant

Figure 2. Neutral stability curves for incremental MLSDC methods with Radau Right points and different time integrators shown after each odd V-cycle

The comparison of the incremental and non-incremental MLSDC formulations for the SI time integrators indicates, that the incremental form is more stable, which underlines that they are not equivalent (compare Figure 3a with 2c or Figure 3b with 2d). Moreover, the non-incremental form takes longer to compute because of the additional operations. Therefore, only the incremental formulation is considered in the following studies.

Remark 9. *In application to space-time problems, a further improvement of stability is expected due to the coarsening in space, leading to lower CFL numbers or, respectively, imaginary parts z_i.*

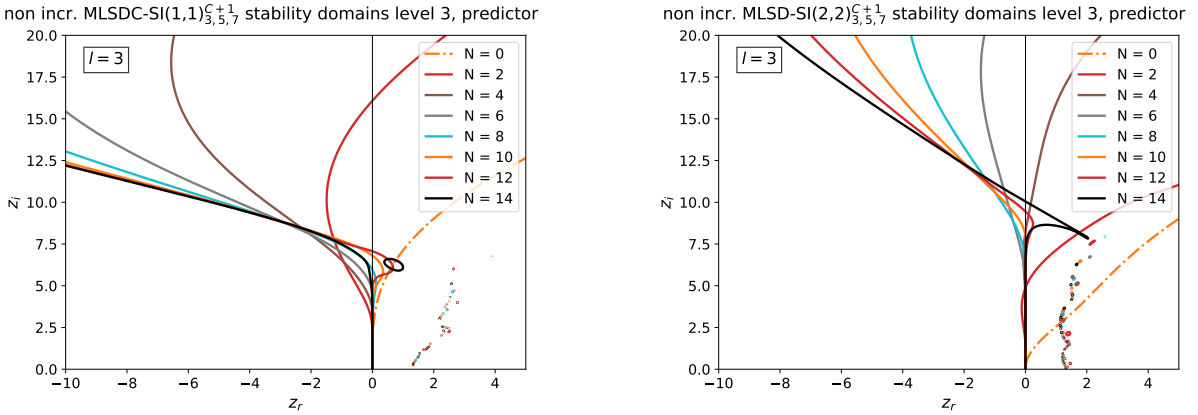

(a) Top level $l = 3$ of MLSDC with SI(1) on all levels, predictor variant

(b) Top level $l = 3$ of MLSDC with SI(2) on all levels, predictor variant

Figure 3. Neutral stability curves for non-incremental MLSDC methods with Radau Right points and different time integrators shown after each odd V-cycle

5.2. Accuracy. Since increasing the number of cycles appears to adversely affect stability, a natural question arises: how many cycles does MLSDC require to achieve convergence? Figure 4 presents accuracy plots for both the incremental and non-incremental methods, showing only the SI(1) and SI(2) time integrators. These methods were selected due to their superior stability. The results correspond to an error tolerance of $\varepsilon = 10^{-6}$ applied uniformly across all levels. Unlike the single-level SDC methods where lines between iterations are expected to be evenly spaced (Appendix B, Figure 15), indicating a uniform increase in order by one per sweep, the plots show that the spacing between lines varies for MLSDC, with convergence initially occurring rapidly before slowing down. Theoretically, standard SDC with Radau Right points and $M = 7$ would require 14 sweeps (Appendix B, Figure 15), whereas MLSDC requires only 9 cycles to achieve the same accuracy for SI(2,2). A comparison of the incremental and non-incremental methods (see Figures 4a with 4e and Figures 4b with 4f) reveals only minor differences, with the incremental approach remaining preferable due to its stability advantages. The FMG_1 variant is observed to perform slightly better compared to the predictor method, particularly in the initial phases of convergence (compare Figure 4a with 4c and Figure 4b with 4d), although both converge after the same number of iterations. The detailed comparison of the convergence between MLSDC and traditional SDC will be continued in subsequent sections.

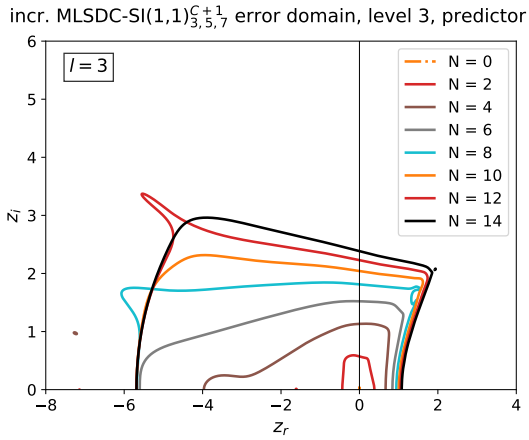

(a) Top level $l = 3$ of incremental MLSDC with SI(1) fon all levels, predictor variant

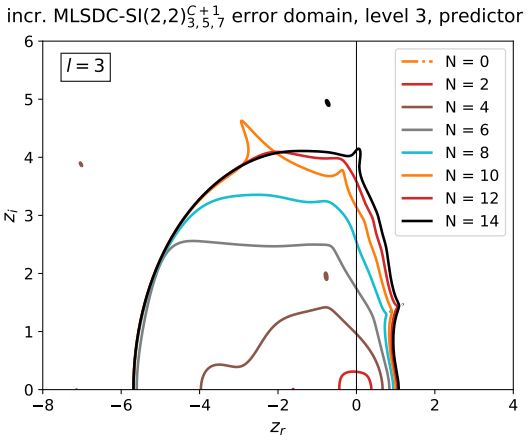

(b) Top level $l = 3$ of incremental MLSDC with SI(2) on all levels, predictor variant

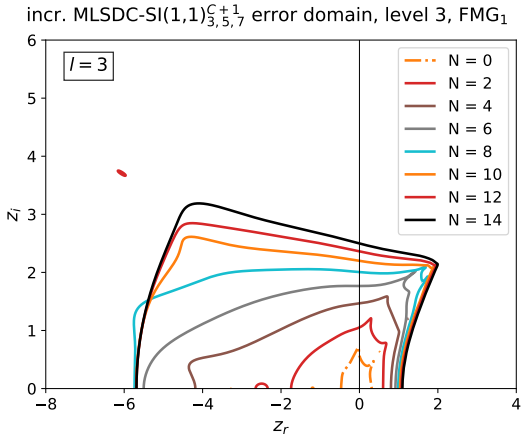

(c) Top level $l = 3$ of incremental MLSDC with SI(1) on all levels, FMG$_1$ variant

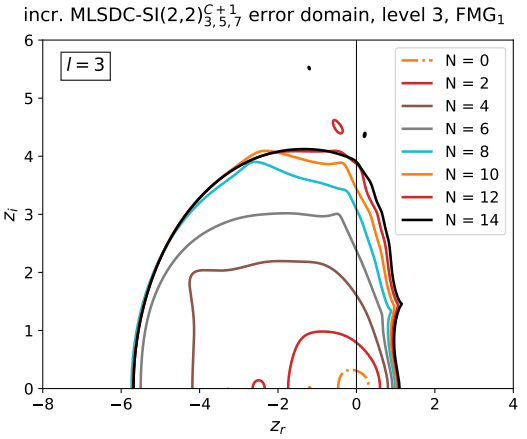

(d) Top level $l = 3$ of incremental MLSDC with SI(2) on all levels, FMG$_1$ variant

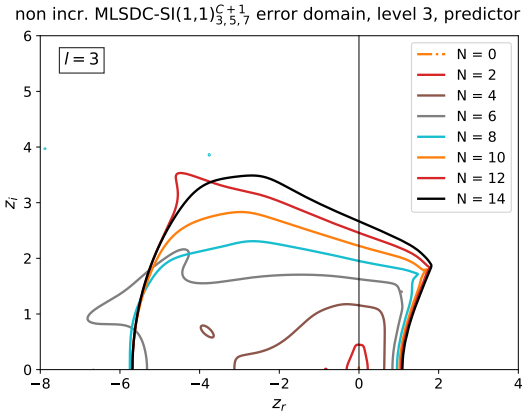

(e) Top level $l = 3$ of non-incremental MLSDC with SI(1) on all levels, predictor variant

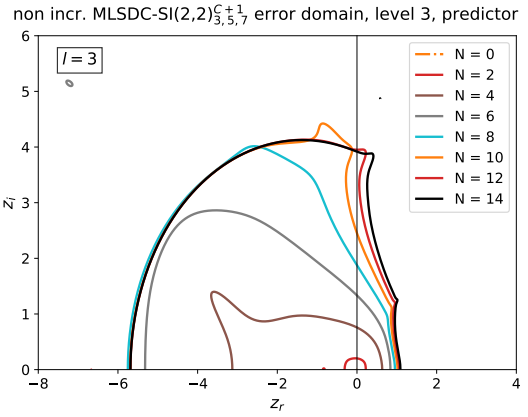

(f) Top level $l = 3$ of non-incremental MLSDC with SI(2) on all levels, predictor variant

Figure 4. Accuracy curves ($\varepsilon = 10^{-6}$) for MLSDC methods with Radau Right points and different time integrators shown after each odd V-cycle for the incremental and non-incremental formulation

6. Spatial discretization

As the investigations now encompass partial differential equations, it is essential to introduce spatial discretization. Spatial discretization is done using a spectral element method, subdividing the domain Ω into a set of discrete elements. This subdivision yields a computational domain denoted by $\Omega_h = \cup\Omega^e$. Within this domain, we define a set of element boundaries Γ_h. These are further divided into Γ_h^{I}, representing the internal boundaries, and Γ_h^{∂}, indicating the external ones. The approximate solution $\boldsymbol{u}_h(x,t)$ is sought within a specific function space at a given time t. This function space is defined as

$$\mathbb{U}_h = \left\{ \boldsymbol{u}_h \in \left[\mathbb{L}^2(\Omega)\right]^d \,:\, \boldsymbol{u}_h|_{\Omega^e} \in \left[\mathbb{P}_P(\Omega^e)\right]^d \quad \forall \Omega^e \in \Omega \right\}. \tag{53}$$

Here, $\mathbb{L}^2$ denotes the space of square-integrable functions, and $\mathbb{P}_P$ refers to the space of polynomials with a degree of at most P. To formulate the problem, weighting functions $\boldsymbol{w}_h$ are introduced. Mathematically, these weighting functions belong to the same function space, $\boldsymbol{w}_h \in \mathbb{U}_h$. For physical consistency, $\boldsymbol{w}_h$ must have dimensions that are reciprocal to those of $\boldsymbol{u}_h$. At the boundary between adjacent elements, the average and jump operators are given by

$$\{\!\{\boldsymbol{u}_h\}\!\} = \frac{\boldsymbol{u}_h^- + \boldsymbol{u}_h^+}{2}, \tag{54}$$

$$[\![\boldsymbol{u}_h]\!] = n^- \boldsymbol{u}_h^- + n^+ \boldsymbol{u}_h^+. \tag{55}$$

Here, $\boldsymbol{u}_h^{\pm}$ are the traces of the corresponding element solutions and $n^{\pm}$ the normals. The discontinuous Galerkin formulation is composed of discrete functionals $\mathcal{M}$ for projection to weighting functions, $\mathcal{F}_{\mathrm{c}}$ for convection, $\mathcal{F}_{\mathrm{d}}$ for diffusion and $\mathcal{F}_{\mathrm{s}}$ for sources. As a result, the right hand side can be written in the form

$$\mathcal{F}(\boldsymbol{w}_h, \boldsymbol{u}_h, \boldsymbol{A}_{\mathrm{d},h}) = \mathcal{F}_{\mathrm{c}}(\boldsymbol{w}_h, \boldsymbol{u}_h) + \mathcal{F}_{\mathrm{d}}(\boldsymbol{w}_h, \boldsymbol{u}_h, \boldsymbol{A}_{\mathrm{d},h}) + \mathcal{F}_{\mathrm{s}}(\boldsymbol{w}_h, \boldsymbol{u}_h, t)\,. \tag{56}$$

For details it is referred to [44]. The diffusion matrix $\boldsymbol{A}_{\mathrm{d},h}$ can be tailored to fit the Euler, SI(1) and SI(2) time integrators introduced above. Moreover, it can be supplemented by an artificial viscosity in order to capture shocks and other discontinuities. In some of the numerical experiments discussed below, we used the artificial viscosity proposed by Persson and Peraire [36] (see also Section 4.3 in [44]).

6.1. Multilevel discretization. In this work, MLSDC is paired with discontinuous Galerkin spectral element method for spatial discretization. Consider a space-time slab (or a space-time element) for a one-level discretization with a domain described by $Q_h = \Omega_h \times T_h$. In this setup, the spatial domain is composed of a union of elements, $\Omega_h = \cup\Omega^e$ each with an element length Δx and basis functions with a polynomial degree of at most P. The temporal domain T_h is similarly divided into intervals T^n, each of length Δt and containing M subintervals as described in the previous sections. As a result, the combined space-time elements are represented by

$$Q^{e,n} = \Omega^e \times T^n. \tag{57}$$

In a multilevel discretization, this structure is extended to multiple levels and denoted by $\boldsymbol{Q}_h = [Q_l]$, where $Q_l = \Omega_l \times T_l$ is the domain for the levels $l = 1 \ldots L$. At each level, the spatial domain is represented as $\Omega_l = \cup\Omega_l^e$, consisting of elements with length Δx_l and polynomial degree P_l. The temporal domain T_l contains intervals T_l^n of length Δt_l and degree M_l. This results in space-time elements at each level denoted by

$$Q_l^{e,n} = \Omega_l^e \times T_l^n. \tag{58}$$

6.2. MLSDC transfer operators. The discrete solution of level l is denoted as $\boldsymbol{u}_l(x,t)$, where the subscript h has been dropped for better readability. For transferring information between subsequent levels, the operators $\mathcal{I}_l$, $\mathcal{P}_l$ and $\mathcal{R}_l$ need to be extended from time to space-time operands. This is achieved by defining corresponding spatial operators and applying them either before or after their temporal counterparts. As the spatial approximation is composed of polynomial basis functions in each element, the design principles are largely identical to the temporal case. One exception appears in the case of 2:1 h-coarsening, where two adjacent fine elements are fused into one on the next coarser level. This coarsening technique may include optional adjustments for discontinuities, such as removing jumps via linear blending (default) or coefficient averaging at interfaces. If embedded interpolation is used for projection $\mathcal{P}_l$, each fine element interpolates to the corresponding part of the coarse element. Contributions to the center of the latter are averaged. With L^2-projection, both fine elements contribute to the whole coarse element. The spatial restriction operator $\mathcal{R}_l$ is again defined as the transpose of the interpolation $\mathcal{I}_{l+1}^t$.

7. Preliminary studies

In this section, the basic functionality and key parameters as well as performance of the MLSDC algorithm is investigated by first examining it with a simple convection-diffusion example (5). To further simplify the initial analysis, only temporal coarsening is considered and one time step performed in $T = [0, 0.1]$ with the time step $\Delta t = 10^{-2}$ being equivalent to the length of the time slab. Periodic boundary conditions are used for the problem. The spatial domain is $x \in \Omega = [0, 1]$ on all levels and the parameters $\nu = 2 \cdot 10^{-2}$ and $v = 1$ are set. The exact solution to the problem is given by:

$$u(x,t) = \sum_{i=1}^{7} a_i \sin\left(\kappa_i(x - s_i - vt)\right) e^{-\kappa_i^2 \nu t}. \tag{59}$$

Equation (59) defines a wave packet comprising various wave numbers κ_i, amplitudes a_i, and phase shifts s_i, as specified in Table 1. The discretization parameters for space and time are

i	1	2	3	4	5	6	7
κ_i	2π	6π	10π	14π	18π	24π	30π
a_i	1.00	1.50	1.80	1.70	1.50	1.30	1.15
s_i	0.00	0.05	0.10	0.15	0.20	0.30	0.18

Table 1. Wave package coefficients

recorded in Table 2 with N_e being the number of elements and n_t the number of time steps. The error should primarily be influenced by the time discretization, ensuring that spatial discretization effects remain minimal. For the first test, a single-level SDC corrector with three different discretizations is compared with a 3 level MLSDC V-cycle with the number of sweeps for the coarse solution $N_c = 2$. Figure 5 shows the L^2 error of the variable $\underline{u}_l$ for each level and after each iteration. The test is done using embedded interpolation (Figure 5a) for the projection operator or L^2-projection (Figure 5b). The iteration count is equivalent to the number of fine grid SDC sweeps. So for the single-level SDC it is the number of sweeps and for the MLSDC method it is the number of cycles + 1 to count the post-sweeping. Zero iterations show the error before applying the SDC corrector or entering the V-cycle. Both methods start at the same point with the predictor solution. The SI(1) method described in Section 3 was used for the predictor and corrector. All

	Space		Time	
	$N_{e,l}$	P_l	$n_{t,l}$	M_l
Level 1	32	15	1	3
Level 2	32	15	1	5
Level 3	32	15	1	7

Table 2. Discretization parameters for tests 1,2 and 4

	Space		Time	
	$N_{e,l}$	P_l	$n_{t,l}$	M_l
Level 1	32	15	1	2
Level 2	32	15	1	4
Level 3	32	15	1	8

Table 3. Discretization parameters for test 3

tests were performed using Radau-Right and Lobatto points as collocation points in time. Overall, Radau Right points yielded better accuracy than Lobatto points throughout all studies, and therefore all results in this document are shown for Radau Right points.

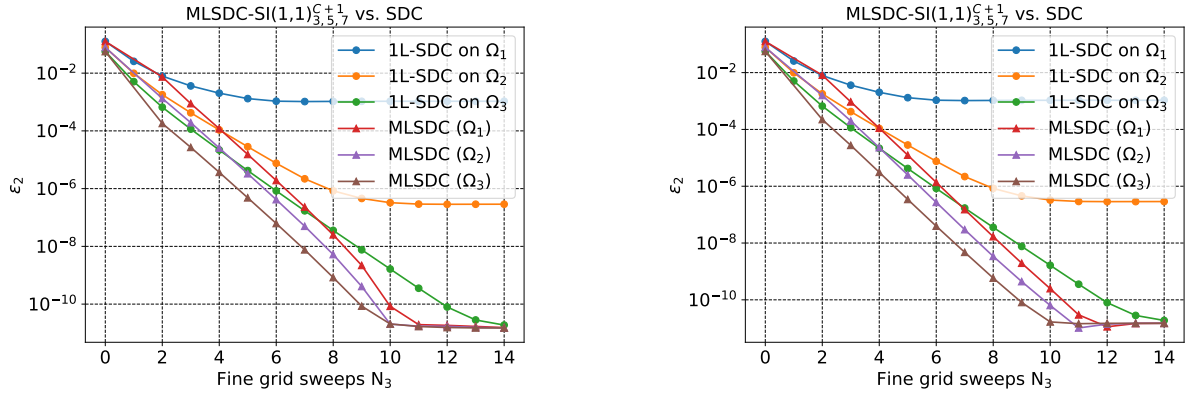

(a) Test 1 - embedded interpolation

(b) Test 1 - L^2-projection

Figure 5. MLSDC V-cycle vs. single-level SDC corrector, number of coarse sweeps $N_c = 2$, predictor variant

Firstly, it can be observed that the MLSDC algorithm converges with fewer iterations and saves SDC sweeps on the finest grid, which was expected. Another observation is that all levels in the V-cycle converge towards the solution on the finest grid, which means that the FAS-RHS works as intended. Note that the SDC Corrector alone for the coarser discretization converges to a higher error. We further observe that MLSDC achieves a faster convergence rate, especially in the first cycle. In contrast, standalone SDC maintains a constant convergence rate of one order per sweep. This behaviour aligns with the accuracy analysis presented in Section 5. In this test, the MLSDC method converges after 9 cycles (10 fine grid sweeps), whereas the single-level SDC needs 14 sweeps. The difference between the L^2-projection and the embedded interpolation is hardly visible for this test case. Since the embedded interpolation still introduces smaller projection errors, it will be the default choice for upcoming tests. Using the restriction operator (36) for variable restriction produced inferior results and is therefore not considered.

Test 2 repeats the first test but with a stronger coarsening in time, compare Table 3. The results for the top levels are shown in Figure 6a. The single-level SDC requires 16 sweeps to reach convergence, while the MLSDC V-cycle converges after 12 cycles, corresponding to 13 fine grid sweeps.

Although MLSDC still converges more efficiently, its advantage over the single-level SDC is noticeably less pronounced in this case, indicating that the coarsening in the time discretization between the levels cannot be too permissive. Following the insights of e.g. [42], a more restrictive temporal coarsening of $M_{l-1} = M_l/2 + 1$ will be approached from now.
The third test repeats test 1 with a different number of coarse sweeps $N_c = 3$. The parameter N_c significantly impacts the convergence rate of the MLSDC method. As N_c increases, the convergence accelerates, highlighting its role as a key factor in achieving faster convergence (compare e.g. the top levels in Figure 5 and Figure 6b). However, it also boosts computational cost and may generate instabilities, necessitating an optimal balance for an efficient runtime.

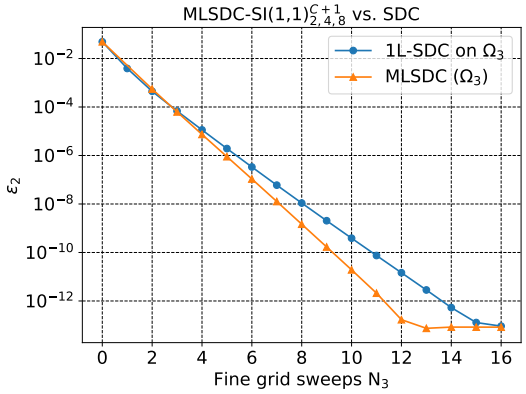

(a) Test 2 - number of coarse sweeps $N_c = 2$, stronger coarsening

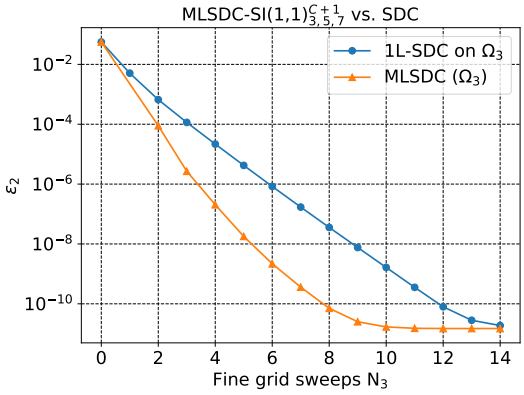

(b) Test 3 - number of coarse sweeps $N_c = 3$

Figure 6. MLSDC V-cycle vs. single-level SDC corrector, predictor variant, embedded interpolation, top level $l = 3$

Note that the performance gain of MLSDC is limited by using the predictor-based start. However, this choice was necessary to ensure a fair comparison with single-level SDC. Test 1 is again repeated for the starting strategies presented in Section 4, see Figure 7. Only errors on the finest level are displayed after each iteration. The constant-value initialization approach yields the worst results, converging one iteration later than the predictor variant. The Cascade variant performs only slightly better than the predictor start, converging after 9 cycles as well. The FMG variants converge the fastest with both FMG_1 and FMG_2 variants almost finishing after 7 cycles. Runtime savings with the FMG_1 variants over the Cascade can be anticipated, as the performed first incomplete V-cycles of the FMG starting variants occur solely between the two coarsest levels. Consequently, the reduction in full V-cycles should compensate for the additional computational cost incurred during the startup phase. A runtime analysis would be relevant at this point; however, measurements taken over a single time step may be neither reliable nor representative and the code is not trimmed for best performance. Thus, a more extensive runtime investigation will be conducted in future work with multiple time steps. For comparable accuracy, the Cascade and constant approaches are expected to be slower than FMG.

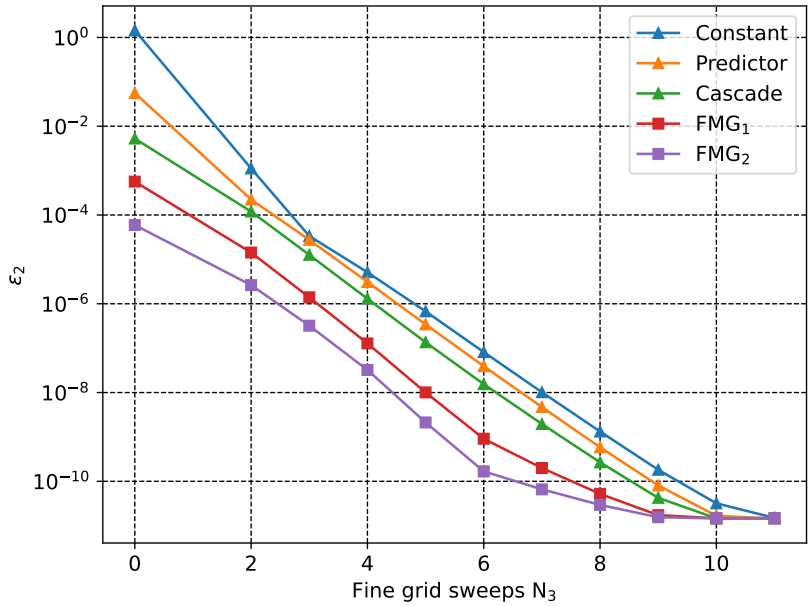

Figure 7. Test 4 - errors for different starting strategies to the MLSDC V-cycle, top level $l = 3$

Based on the observations and analysis, a set of default parameters is established for the subsequent tests. The number of coarse correction sweeps is set to $N_c = 2$, as this configuration provides good convergence properties while maintaining stability. For projection, embedded interpolation is chosen over L^2-projection due to its slightly favourable accuracy. Regarding the MLSDC starting strategy, the FMG_1 approach is selected for two-level and multilevel configurations. Note that the FMG_1 approach is equivalent to the Cascade strategy for a two-level configuration. The incremental formulation is preferred over the non-incremental method, as it proved to be more stable. The time integration method is fixed to SI(2), based on insights from the Dahlquist-type analysis. Thus, unless explicitly stated otherwise, all subsequent tests are conducted using $N_c = 2$, embedded interpolation as the projection method, the Cascade strategy or FMG_1 for initialization, and the incremental formulation. Furthermore, post-sweeping is enabled by default.

8. Numerical Experiments

The accuracy and stability of the MLSDC method are extensively evaluated through numerical experiments on linear convection-diffusion, Burgers, and compressible flow problems in this section. Two central questions arise in the context of MLSDC: First, does the method retain the same stability properties as single-level SDC when applied to partial differential equations - or potentially even improves stability due to the combined space-time coarsening? Second, how rapidly does MLSDC converge in practice for PDEs with space-time coarsening, and to what extent does it reduce the number of iterations on the fine grid compared to standard SDC? For the upcoming tests, the CFL number is defined as

$$CFL = \frac{\Delta t \, \lambda_{\text{c,max}}}{\Delta x}, \tag{60}$$

where the characteristic length scale Δx is following the approach in [7, Sec. 7.3.3] and chosen as

$$\Delta x = \frac{\Delta x^e}{2\delta}\,. \tag{61}$$

There, $\delta \sim P^2$ denotes the largest eigenvalue of the convection problem with unit velocity and one-sided Dirichlet boundary conditions in the standard element $[-1, 1]$. The CFL number is determined from the initial conditions and on the finest grid, unless otherwise stated.

8.1. Convection-diffusion. The numerical experiments in this section build upon the tests presented in [44, Sec. 6]. The initial set of test problems focusses on the convection-diffusion equation (5), with the exact solution given by the same wave packet as discussed in Section 7. The tests are performed in the periodic domain $\Omega = [0, 1]$ and a time interval $[0, 5]$, i.e. five periods of the longest wave. The discretization parameters for the first test can be taken from Table 4, the number of coarse sweeps $N_c = 2$. We first consider a constant velocity of $v = 1$ and diffusivity $\nu = 10^{-3}$.

	Space		Time
	$N_{e,l}$	P_l	M_l
Level 1	16	15	3
Level 2	32	15	5
Level 3	64	15	7

Table 4. Discretization parameters for the convection-diffusion tests

Figure 8 compares the single-level SDC method using the fine grid discretization (level 3) with MLSDC. The L_2 error of the fine grid is shown after each cycle of the MLSDC method (red markers) and after each sweep for SDC (blue markers) for different CFL numbers. The markers specify the number of fine grid sweeps. The $C+1$ notation indicates C V-cycles + 1 fine grid sweep to account for the post-sweeping. The error is displayed after each iteration, since there is no theoretical maximum number of iterations required for the MLSDC method to reach convergence. The CFL number on the finest grid is initially set to 64 and is subsequently reduced by a factor of 2 down to $1/2$.

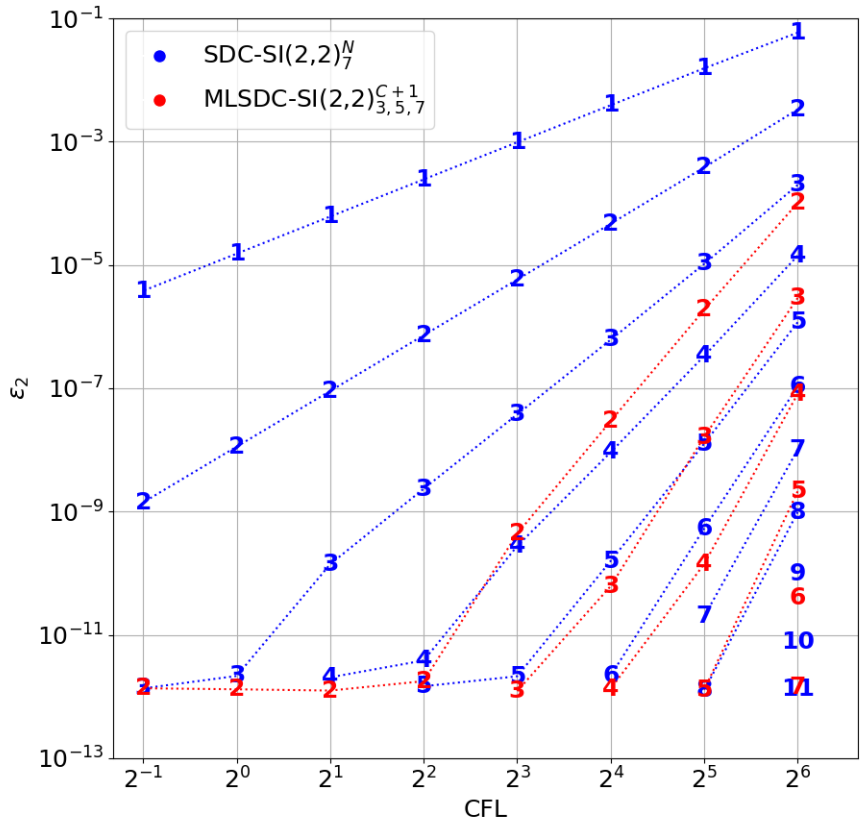

Figure 8. L_2 errors over CFL numbers SDC$_7^N$ vs. MLSDC$_{3,5,7}^{C+1}$ for convection-diffusion and $\nu = 10^{-3}$, top level, markers indicate the number of fine grid sweeps

As expected, the errors decrease after each iteration, whether it corresponds to a sweep in SDC or a cycle in the MLSDC method. There are clear savings in fine grid iterations for MLSDC. For CFL numbers of 0.5 to 4, it requires only one full cycle to converge and hence two fine grid sweeps. For $CFL = 64$, MLSDC converges after 6 cycles, while the SDC method requires 11 sweeps. The advantage of MLSDC becomes more pronounced as the number of needed iterations to converge increases. As a result, the benefits of MLSDC are more apparent for higher CFL numbers. No stability issues were encountered in any of the cases tested with $\nu = 10^{-3}$.

The second test considers the case of pure convection $\nu = 0$ in the time interval $[0, 5]$. The discretization parameters are identical to the previous test. Figure 9 compares the single-level SDC method to a two-level method (level 2 and 3) with the Cascade start. For clarity, only the iteration count at which the method converges for a given CFL number is shown. A test case is considered converged when the relative change in the L_2 error between two iterations falls below 10 percent. This criterion is applied consistently across all subsequent experiments. The general results for $\nu = 0$ are consistent with those observed for $\nu = 10^{-3}$, although more iterations are generally required to achieve convergence. Across all CFL numbers, MLSDC exhibits faster convergence.

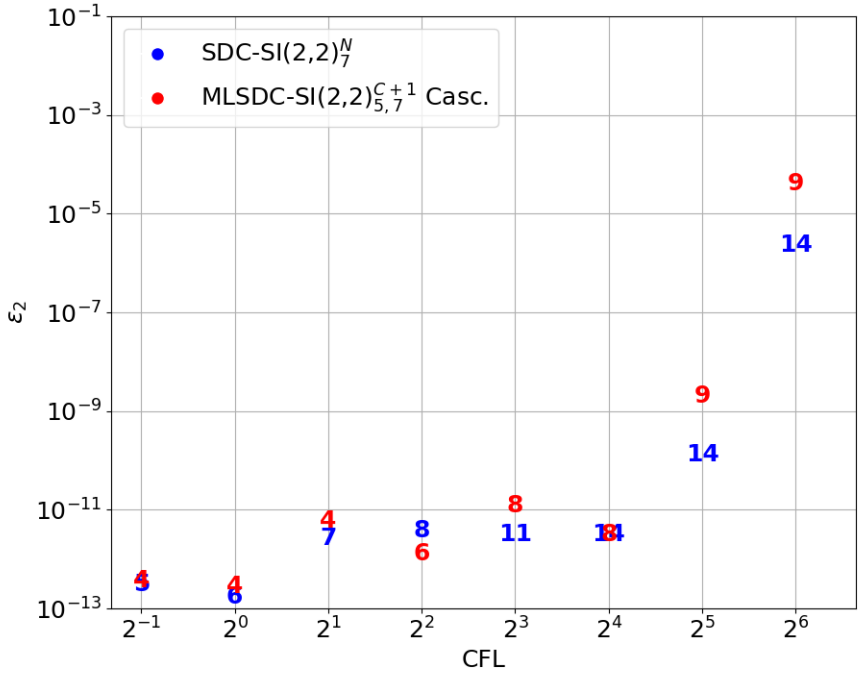

Figure 9. L_2 errors over CFL numbers SDC$_7^N$ vs. MLSDC$_{5,7}^{C+1}$ for convection-duffusion and $\nu = 0$, top level, markers indicate the number of fine grid sweeps

For instance, at $CFL = 32$ and $CFL = 64$, it converges after 8 cycles compared to 14 sweeps required by the single-level SDC method. However, for larger time steps, the method tends to converge to a higher terminal error, despite the reduced number of iterations. Stability issues are observed for both methods, and these become more pronounced in MLSDC as the number of coarse-grid levels, N_c, increases. Applying coarsening in both time and space mitigates these issues to some extent, as the coarse-grid CFL number is reduced. Up to a CFL number of 16, the method remains stable. Beyond this threshold, it becomes unstable if more than 9 cycles are performed for this problem. Another key observation is that the resolution gap between levels must not be too large. Otherwise, transfer errors between levels increase significantly, adversely affecting both stability and accuracy. In particular, the coarsest level is critical for determining the overall performance of the MLSDC method. Using a 3-level FMG$_1$ variant with the discretization parameters from Table 4 results in faster convergence for smaller CFL numbers. However, for higher CFL values, stability and accuracy degrade. This issue will be investigated in more detail in the subsequent test cases.

8.2. Burgers equation. The Burgers equation (6) presents a numerical challenge due to its nonlinear dynamics, which can lead to the formation of shock waves and discontinuities. Additionally, variations in the convective Jacobian matrix cause changes in diffusivity within the semi-implicit methods devised in this study. The test case considered here relates to the moving front solution

$$u(x,t) = 1 - \tanh\left(\frac{x + 0.5 - t}{2\nu}\right) \tag{62}$$

for $x \in [-1, 1]$ and $t \in [0, 0.1]$, see [22]. Assuming a diffusivity of $\nu = 10^{-2}$ yields a thin advancing front (Figure 10), which is expensive to resolve numerically.

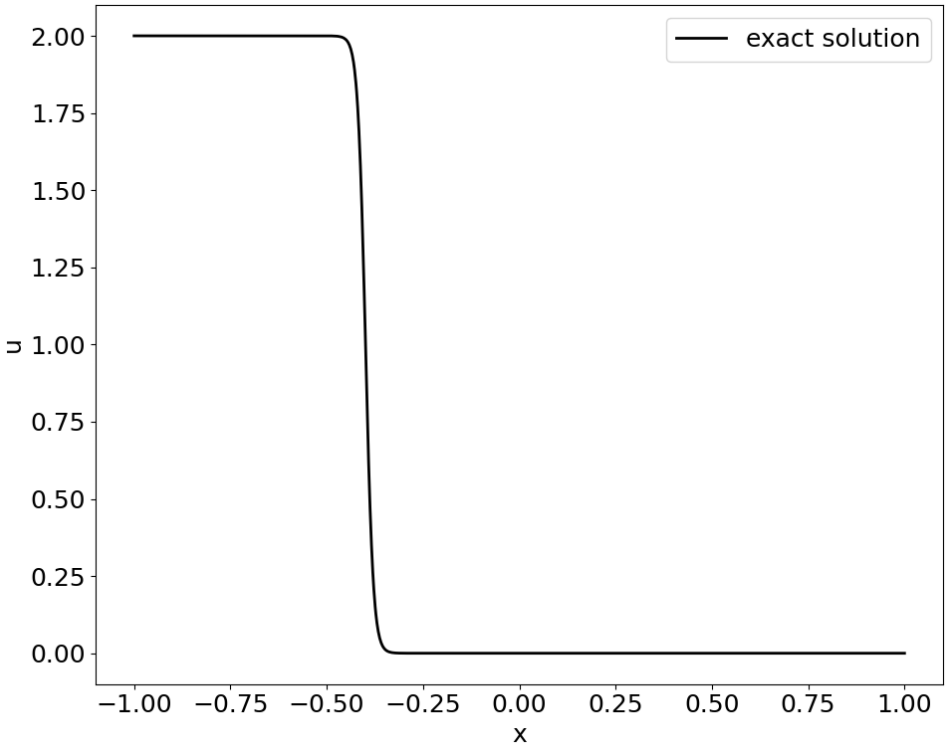

Figure 10. Burgers moving front with $\nu = 10^{-2}$ at t=0.1

We consider two cases: (1) the front is spatially well-resolved on all levels, including the coarsest; (2) the front is spatially under-resolved on all levels, including the finest. To capture the front and to avoid unphysical oscillations in the underresolved case, the artificial diffusivity of Persson and Peraire is used with parameters $\kappa_s = 0.5$ and $c_s = 0.5$, see [36] and [44] for details. Figure 11 displays the L_2 errors achieved with the different methods for the problem. The markers in the figures indicate the number of fine grid sweeps, as listed in Table 5 and 6.

We first consider the highly resolved test case. Table 5 presents the number of fine grid operations required to achieve convergence across various CFL numbers (compare Figure 11a). The fine grid CFL number is kept constant across the two different spatial resolutions. As a result, for a given CFL number, the corresponding time step/slab size differs between the test cases. In this setting, both spatial h-coarsening and p-coarsening perform without any issues. However, h-coarsening proves to be more effective, as the L_2 error on the coarsest level is lower compared to that obtained with p-coarsening in this test. The iteration savings achieved by MLSDC are significant. For certain values of the CFL number, it requires less than half as many fine grid sweeps as single-level SDC. At lower CFL numbers, MLSDC often fully converges with just one cycle, which is equivalent to only two fine grid iterations. The results for the starting strategies described in Section 7 are reproduced as well. It should also be mentioned that, in the cases with space-time coarsening, the embedded interpolation method generally outperformed the L_2-projection as a variable projection method. In some instances, this led to significantly lower L_2 errors after a fixed

Method				CFL							
	N_e	P	Start	0.5	1	2	4	8	16	32	64
SDC-SI(2,2)$_7^N$	200	15	-	3	4	4	5	6	7	11	14
MLSDC-SI(2,2)$_{3,5,7}^{C+1}$	$\{200, 200, 200\}$	$\{15, 15, 15\}$	FMG$_1$	2	2	2	2	2	4	6	9
	$\{50, 100, 200\}$	$\{15, 15, 15\}$	FMG$_2$	2	2	2	2	2	3	6	9
	$\{50, 100, 200\}$	$\{15, 15, 15\}$	FMG$_1$	2	2	2	2	2	4	6	9
	$\{50, 100, 200\}$	$\{15, 15, 15\}$	Casc.	2	2	2	2	3	5	7	10
	$\{200, 200, 200\}$	$\{5, 10, 15\}$	FMG$_1$	3	4	4	4	4	9	9	10

Table 5. Number of needed fine grid iterations until convergence for different CFL numbers at high spatial resolution

number of iterations, sometimes by an order of magnitude.
If all levels suffer from poor resolution (Figure 11b and Table 6), the MLSDC still performs stably, although the benefits it provides become less pronounced. The solution projected from the

Method				CFL							
	N_e	P	Start	0.5	1	2	4	8	16	32	64
SDC-SI(2,2)$_7^N$	40	8	-	2	2	3	4	6	8	8	8
MLSDC-SI(2,2)$_{3,5,7}^{C+1}$	$\{40, 40, 40\}$	$\{8, 8, 8\}$	FMG$_1$	2	2	2	2	3	6	6	6
	$\{10, 20, 40\}$	$\{8, 8, 8\}$	FMG$_1$	2	2	3	3	4	6	6	6
	$\{40, 40, 40\}$	$\{2, 4, 8\}$	FMG$_1$	2	2	3	4	5	7	7	7

Table 6. Number of needed fine grid iterations until convergence for different CFL numbers at low spatial resolution

finer levels cannot be properly represented on the poorly resolved coarser levels. This also seems to affect the FAS RHS and the coarse-to-fine correction becomes inefficient. For MLSDC with h- or p-coarsening, this leads to slower convergence and higher terminal L_2 errors compared to the single-level SDC solution for high CFL numbers. Moreover, it was observed that an underresolved solution on the coarse level can introduce jumps or oscillations in the numerical solution. In the context of the Cascade and FMG starting strategies, these artifacts are subsequently interpolated to the next finer level, resulting in unfavourable initial values for the MLSDC method. This, in turn, can delay convergence or degrade the overall efficiency of the method. As a practical workaround, the starting values are smoothed prior to interpolation, e.g. by averaging out jumps across element interfaces on the coarse level. This procedure is applied in all Burgers moving front test cases. The issues associated with an unresolved coarse level are known to the authors. Potential remedies, such as the use of filters and smoothing of the starting solutions, are already under investigation, but beyond the scope of this study. These limitations are less restrictive in cases with higher diffusion, as the solution is smoother in such scenarios.

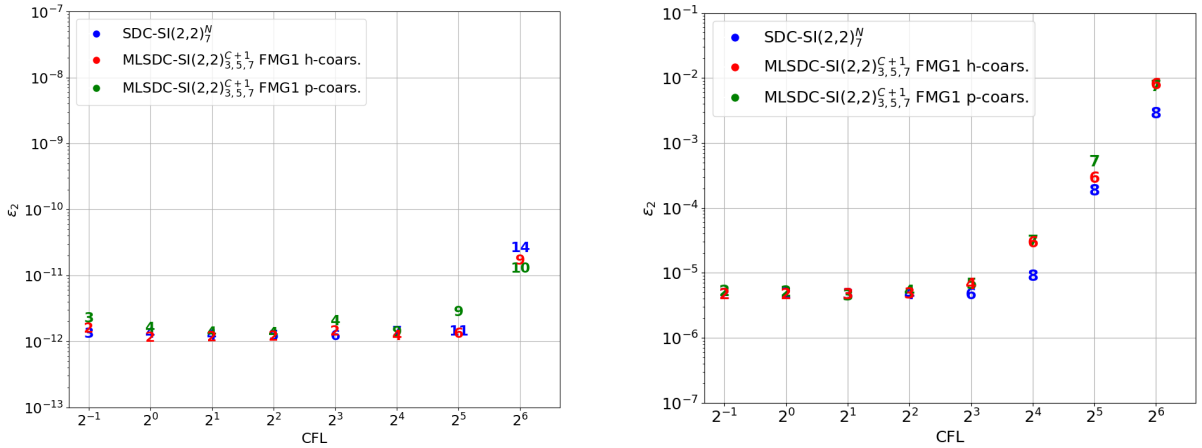

(a) high spatial resolution (1)

(b) low spatial resolution (2)

Figure 11. L_2 errors over CFL numbers SDC$_7^N$ vs. MLSDC$_{3,5,7}^{C+1}$ for Burgers moving front and $\nu = 10^{-2}$, top level, markers indicate the number of fine grid sweeps

8.3. Euler and Navier-Stokes equations. Now some compressible flow problems are investigated. The fluid is modeled as a perfect gas and exhibits properties corresponding to air, with a specific gas constant $R = 287.28$ and a heat capacity ratio $\gamma = 1.4$, under standard conditions and assuming SI units. The first problem describes an acoustic wave traveling downstream in a uniform flow characterized by a Mach number $Ma = 0.1$, ambient pressure $p_\infty = 1000$, temperature $T_\infty = 300$, dynamic viscosity $\eta = 10^{-5}$ and Prandtl number $Pr = 0.75$. This wave is initialized by superimposing the periodic velocity perturbation, defined mathematically by the equation:

$$v'(x) = \hat{v}\sin(2\pi x), \tag{63}$$

with an amplitude of $\hat{v} = 10^{-2}a_\infty$, where $a_\infty \approx 347.36$ is the speed of sound in the undisturbed fluid. Assuming an isotropic initial state, the inital temperature is given by

$$T_0(x) = \frac{1}{\gamma R}\left(a_\infty + \frac{\gamma - 1}{2}v'\right)^2, \tag{64}$$

the pressure by

$$p_0(x) = p_\infty\left(\frac{T}{T_\infty}\right)^{\gamma/(\gamma-1)}, \tag{65}$$

and the velocity by

$$v_0(x) = Ma\, a_\infty + v'(x)\,. \tag{66}$$

It is to be noted, that the amplitude of the wave is sufficiently large to trigger non-linear steepening effects in the wave dynamics. Conversely, the impact of viscous damping is considered negligible owing to the high Reynolds number $Re = \rho_\infty a_\infty / \eta \approx 4 \times 10^5$. The progression of the wave is studied within a periodic domain $\Omega = [0, 1]$, from $t = 0$ to $t_{\text{end}} = 2.619 \times 10^{-2}$. This time frame approximately covers 10 convective units. The discretization parameters employed in the study are detailed in Table 7.

	Space		Time
	$N_{e,l}$	P_l	M_l
Level 1	6	8	3
Level 2	12	8	5
Level 3	12	15	7

Table 7. Discretization parameters for the acoustic wave test

Since no exact solution is available, the TVD-RK3 method of Shu and Osher [39] with $\Delta t \approx 10^{-7}$ or $CFL \approx 0.019$ serves as a reference. The first test corresponds to a 2-level MLSDC method (level 2 and level 3 from Table 7) with a Cascade start vs. a single-level SDC method. The results can be seen in Figure 12. The MLSDC method can stably solve the CNS acoustic wave problem for CFL numbers up to 494. After 7 cycles (8 fine grid sweeps), it already shows better agreement with the reference than single-level SDC after 11 sweeps, especially for high CFL numbers (494 and 258).

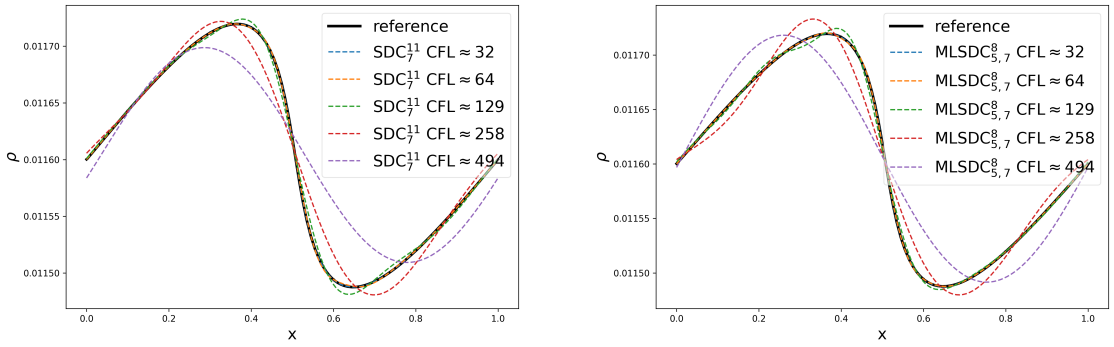

(a) SDC-SI(2,2)$_7^{11}$ **(b)** MLSDC-SI(2,2)$^8_{5,7}$

Figure 12. Acoustic wave density distributions obtained with SDC-SI(2,2)$_7^{11}$ vs MLSDC-SI(2,2)$^8_{5,7}$

The second test considers a three-level discretization using the FMG$_1$ starting variant, see Figure 13. Compared to the two-level method, this setup achieves even greater iteration savings for lower CFL numbers. However, the method encounters difficulties in accurately solving the problem for greater CFL numbers, particularly at $CFL = 494$. It may be suspected that this issue is related to an insufficient temporal resolution on the coarse level, which worsens when the CFL number increases. Increasing the number of cycles does not improve the solution; instead, it introduces slight instabilities. The three-level method still successfully solves the problem for CFL numbers up to 258, which remains a notable result. In summary, the three-level MLSDC offers clear advantages at small CFL numbers. At larger CFL values, however, the limitations due to poor resolution on the coarsest grid become apparent.

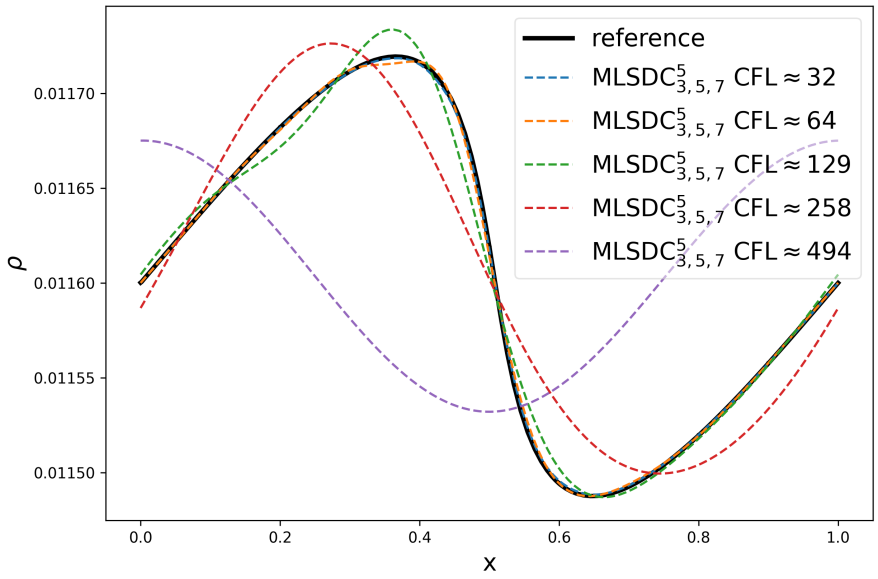

Figure 13. Acoustic wave density distributions obtained with MLSDC-SI(2,2)$^5_{3,5,7}$ FMG$_1$ variant

The second example is Sod's shock tube problem for the Euler equations with initial conditions [40]

$$\rho = 1, \quad p = 1, \quad v = 0 \quad \text{if} \quad x < 0.5 \tag{67a}$$
$$\rho = 0.125, \quad p = 0.1, \quad v = 0 \quad \text{if} \quad x \geq 0.5 \tag{67b}$$

to solve on $\Omega = [0, 1]$ until $t = 0.2$. For the numerical studies, the domain is divided into 80 elements of degree 5 on the finest level. The discretization parameters for the test can be taken from Table 8, the number of coarse sweeps $N_c = 2$.

	Space		Time	
	$N_{e,l}$	P_l	$n_{t,l}$	M_l
Level 1	80	3	32	5
Level 2	80	5	32	7

Table 8. Discretization parameters for the shock-tube test

The artificial diffusivity of Persson and Peraire [36] is used with $\kappa_s = 2$ and $c_s = 0.4$ to capture the evolving shock and the contact discontinuity. Figure 14 shows the velocity v obtained with SDC-SI(2,2)$^N_7$ and MLSDC-SI(2,2)$^C_{5,7}$ using 32 time steps ($CFL \approx 7$) after different numbers of iterations. The MLSDC used the Cascade starting strategy. The TVD-RK3 with 10^5 steps or $\Delta t = 2 \times 10^{-6}$ serves as a reference. The shock tube problem could only be solved stably with spatial coarsening,

using $P_l = 5$ on all levels led to instability, likely due to an excessively large coarse grid CFL number. With 32 time steps, the agreement with the reference solution is already very good. Although both SDC and MLSDC appear to resolve the wave front around $x \approx 0.85$ equally well, there are overshooting oscillations in the lower part of the domain in the SDC solution, which can not be observed in the MLSDC method. In addition, the MLSDC method converges toward the reference solution more rapidly.

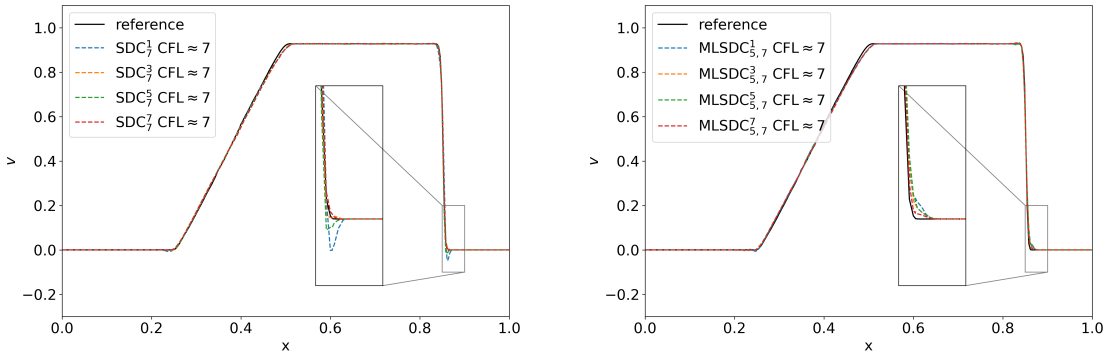

(a) SDC-SI(2,2)$_7^N$ **(b)** MLSDC-SI(2,2)$^C_{5,7}$

Figure 14. Shock Tube velocity distributions obtained with SDC-SI(2,2)$_7^N$ vs MLSDC-SI(2,2)$^C_{5,7}$ at $CFL \approx 7$

8.4. Notes on runtime. The focus of this paper was the stability, convergence and accuracy of the SI-MLSDC method. In our comparative analysis, we specifically examine the iterations executed on the fine grid for the single-level SDC and the MLSDC. First conducted numerical studies reveal that the MLSDC does not necessarily always currently achieve runtime savings for global refinement and 1D test cases. At this point, a preliminary estimate of the runtime shall be provided.

The computational model utilized in this small analysis is intentionally simplified. These simplifications include the absence of factors such as communication overhead and the exclusion of additional runtime overhead from the transfer operators in MLSDC. In addition, all implicit equations are currently being iterated to convergence at all levels (e.g. within the diffusion solver). However, this streamlined model allows for a clearer examination of the core computational elements without the confounding effects of more complex system interactions. For estimating the runtime of single-level SDC implementations, we suggest the following:

$$t_{\text{Run,SDC}} \approx c_R \times (P+1) \times N_e \times M \times n_t \times N\,, \tag{68}$$

where c_R is a coefficient representing the runtime associated with a single operation within the SDC framework, encompassing activities such as the solution of implicit parts and spatial discretization. Additionally, N denotes the number of sweeps performed. This formulation provides a foundational estimate, albeit approximate. The computational efficiency of the MLSDC method

can be captured through the following modeled runtime estimate:

$$t_{\text{Run,MLSDC}} \approx \sum_{l=2}^{L} c_R \times (P_l + 1) \times N_{e,l} \times M_l \times n_{t,l} \times (C + 1) + c_R \times (P_1 + 1) \times N_{e,1} \times M_1 \times n_{t,1} \times N_c \times C \tag{69}$$

In scenarios where only p-refinement in space and time is applied, and the standalone SDC utilizes the fine grid discretization, a two-level MLSDC would offer a time-saving advantage under the condition:

$$(P_2 + 1) \times M_2 \times N > (P_2 + 1) \times M_2 \times (C + 1) + (P_1 + 1) \times M_1 \times N_c \times C \tag{70}$$

For a simplified assumption, $N_c = 2$, P_1 and P_2 are high polynomial orders and $P_1 = P_2/2$ and $M_1 = M_2/2$, the MLSDC approach becomes beneficial if it converges after fewer than $C < 2/3 \times (N-1)$ cycles. It is noteworthy that in three-dimensional applications, the advantages of utilizing a less expensive coarse grid become significantly more pronounced. However, the overhead associated with the MLSDC framework such as transfer operators, which scales with problem size, is not accounted for.

9. Conclusions

This paper introduces a new class of robust semi-implicit multilevel spectral deferred correction (SI-MLSDC) methods, characterized by excellent stability properties. The core foundation of these methods is the use of SI time integrators, which employ a semi-implicit splitting of the convection term inspired by the Lax-Wendroff method while treating diffusion and source terms implicitly, following the approach in [44]. The stability and accuracy of the proposed methods are thoroughly analyzed in Section 5 using a Dahlquist-type problem. The SI(2,2) time integrator demonstrated the best stability and accuracy properties. In contrast, the IMEX Euler method exhibited the poorest performance and was therefore not considered further in this study. Moreover, the non-equivalence between the incremental and non-incremental MLSDC formulations is shown, and the former exhibits favourable stability properties. Among the aspects considered in this work is a detailed presentation and discussion of transfer operators, particularly the choice between L^2-projection and embedded interpolation as a projection method. To further assess their numerical performance, the SI-MLSDC method was applied to high-order discontinuous Galerkin formulations of one-dimensional conservation laws, demonstrating high-order accuracy in space and time. In the numerical studies, the convergence properties of the proposed SI-MLSDC methods were examined, along with key influencing factors such as different starting strategies (constant, cascadic, predictor, FMG) and the number of coarse sweeps, N_c. Tests using the convection-diffusion equation highlight the excellent stability and accuracy of SI-MLSDC, remaining stable for CFL numbers up to at least 64. It is demonstrated, that the proposed SI-MLSDC method reduces the number of iterations required on the fine grid, with these savings becoming even more pronounced for the Burgers moving front problem. For instance, for certain CFL numbers, MLSDC-SI(2,2)$^{C+1}_{3,5,7}$ FMG required less than half the number of fine-grid sweeps compared to SDC-SI(2,2)$^{N}_{7}$. Similar iteration savings on the fine grid and faster convergence were also observed for other non-linear problems, including the Euler and Navier-Stokes equations. In some cases, stabilization techniques were necessary near discontinuities. This included artificial diffusion methods as well as a combined p-coarsening strategy in both space and time, rather than p-coarsening in time alone, to reduce the CFL number on the coarse grid. Examples such as the Shock Tube test

case illustrate this need. Issues related to an under-resolved problem on the coarsest grid were identified, and potential solution strategies were discussed. These observations may align with the insights regarding an overly permissive coarsening strategy. A solution to this limitation is under investigation. While the current implementation does not yet yield direct runtime savings, partly due to the code not being optimized for performance, future improvements are expected with the introduction of local adaptivity in combination with reliable error estimators and the application to three-dimensional problems. At this stage, MLSDC provides the necessary infrastructure for further advancements and already displays considerable fine grid operation savings while remaining stable for a wide variety of problems. The next steps involve local refinement in space-time, following the ideas of Emmett et al. [15] but with arbitrary high orders, more refined error estimators, improved stability, and greater flexibility.

Data Availability

The datasets generated during the current study are available from the corresponding author on reasonable request.

Funding

Funding by German Research Foundation (DFG) in frame of the project STI 57/9-1 is gratefully acknowledged. The authors would like to thank ZIH, TU Dresden, for the provided computational resources. Open Access funding is enabled and organized by Projekt DEAL.

Ethics declarations

The authors declare that they has no known competing financial interests or personal relationships that could have appeared to influence the work reported in this paper.

References

[1] I. Akramov, S. Götschel, M. Minion, D. Ruprecht, and R. Speck. Spectral deferred correction methods for second-order problems. *SIAM Journal on Scientific Computing*, 46(3): A1690–A1713, May 2024. ISSN 1095-7197. doi: $10.1137/23\mathrm{m}1592596$. URL `http://dx.doi.org/10.1137/23M1592596`.

[2] U. M. Ascher, S. J. Ruuth, and R. J. Spiteri. Implicit-explicit Runge-Kutta methods for time-dependent partial differential equations. *Applied Numerical Mathematics*, 25(2-3):151–167, 1997. doi: $10.1016/\mathrm{s}0168\text{-}9274(97)00056\text{-}1$.

[3] A. Baeza, R. Bürger, M. d. C. Martí, P. Mulet, and D. Zorío. On approximate implicit taylor methods for ordinary differential equations. *Computational and Applied Mathematics*, 39(4), 2020. doi: $10.1007/\mathrm{s}40314\text{-}020\text{-}01356\text{-}8$.

[4] F. Bassi, L. Botti, A. Colombo, A. Ghidoni, and F. Massa. Linearly implicit Rosenbrock-type Runge–Kutta schemes applied to the discontinuous Galerkin solution of compressible and incompressible unsteady flows. *Computers & Fluids*, 118:305–320, 2015. doi: $10.1016/\mathrm{j}.\mathrm{compfluid}.2015.06.007$.

[5] M. Bolten, D. Moser, and R. Speck. A multigrid perspective on the parallel full approximation scheme in space and time, 2016. URL `https://arxiv.org/abs/1603.03586`.

[6] A. Brandt and O. E. Livne. *Multigrid Techniques*. Society for Industrial and Applied Mathematics, 2011. doi: $10.1137/1.9781611970753$. URL `https://epubs.siam.org/doi/abs/10.1137/1.9781611970753`.

[7] C. Canuto, M. Y. Hussaini, A. Quarteroni, and T. A. Zang. *Spectral Methods. Fundamentals in Single Domains*. Springer Berlin Heidelberg, 2011. ISBN 3540307257.

[8] D. Cavaglieri and T. Bewley. Low-storage implicit/explicit Runge-Kutta schemes for the simulation of stiff high-dimensional ODE systems. *Journal of Computational Physics*, 286:172–193, 2015. doi: 10.1016/j.jcp.2015.01.031.

[9] A. Christlieb, M. Morton, B. Ong, and J.-M. Qiu. Semi-implicit integral deferred correction constructed with additive Runge–Kutta methods. *Communications in Mathematical Sciences*, 9(3):879–902, 2011. doi: 10.4310/cms.2011.v9.n3.a10.

[10] A. J. Christlieb, Y. Liu, and Z. Xu. High order operator splitting methods based on an integral deferred correction framework. *Journal of Computational Physics*, 294:224–242, 2015. doi: 10.1016/j.jcp.2015.03.032.

[11] G. Dahlquist. A special stability problem for linear multistep methods. *BIT Numerical Mathematics*, 3:27–43, 1963. URL https://api.semanticscholar.org/CorpusID:120241743.

[12] P. Deuflhard and F. Bornemann. *Scientific Computing with Ordinary Differential Equations*. Springer New York, 2002. ISBN 9780387215822. doi: 10.1007/978-0-387-21582-2.

[13] A. Dutt, L. Greengard, and V. Rokhlin. Spectral deferred correction methods for ordinary differential equations. *Bit Numerical Mathematics*, 40(2):241–266, 2000. doi: 10.1023/a:1022338906936.

[14] M. Emmett and M. Minion. Toward an efficient parallel in time method for partial differential equations. *Communications in Applied Mathematics and Computational Science*, 7(1):105 – 132, 2012. doi: 10.2140/camcos.2012.7.105. URL https://doi.org/10.2140/camcos.2012.7.105.

[15] M. Emmett, E. Motheau, W. Zhang, M. Minion, and J. B. Bell. A fourth-order adaptive mesh refinement algorithm for the multicomponent, reacting compressible navier–stokes equations. *Combustion Theory and Modelling*, 23(4):592–625, Jan. 2019. ISSN 1741-3559. doi: 10.1080/13647830.2019.1566574. URL http://dx.doi.org/10.1080/13647830.2019.1566574.

[16] N. Fehn, W. A. Wall, and M. Kronbichler. On the stability of projection methods for the incompressible Navier-Stokes equations based on high-order discontinuous Galerkin discretizations. *Journal of Computational Physics*, 351:392–421, 2017. doi: 10.1016/j.jcp.2017.09.031.

[17] P. Frolkovič and M. Žeravý. High resolution compact implicit numerical scheme for conservation laws. *Applied Mathematics and Computation*, 442:127720, 2023. doi: 10.1016/j.amc.2022.127720.

[18] S. Gottlieb and D. Ketcheson. *Time Discretization Techniques*, pages 549–583. Elsevier, 2016. doi: 10.1016/bs.hna.2016.08.001.

[19] E. Hairer and G. Wanner. *Solving Ordinary Differential Equations II*. Springer Berlin Heidelberg, 1996. doi: 10.1007/978-3-642-05221-7.

[20] E. Hairer, S. P. Nørsett, and G. Wanner. *Solving Ordinary Differential Equations I*. Springer Berlin Heidelberg, 1993. doi: 10.1007/978-3-540-78862-1.

[21] F. P. Hamon, M. Schreiber, and M. L. Minion. Multi-level spectral deferred corrections scheme for the shallow water equations on the rotating sphere. *Journal of Computational Physics*, 376:435–454, 2019. ISSN 0021-9991. doi: https://doi.org/10.1016/j.jcp.2018.09.042. URL https://www.sciencedirect.com/science/article/pii/S0021999118306442.

[22] J. S. Hesthaven and T. Warburton. *Nodal Discontinuous Galerkin Methods*. Springer, 2008.

[23] I. Huismann, J. Stiller, and J. Fröhlich. Cascadic multigrid in a spectral-element context. *PAMM*, 16(1):841–842, 2016.

[24] G. E. Karniadakis, M. Israeli, and S. A. Orszag. High-order splitting methods for the incompressible Navier-Stokes equations. *Journal of Computational Physics*, 97(2):414–443, 1991. doi:

10.1016/0021-9991(91)90007-8.

[25] C. A. Kennedy and M. H. Carpenter. Additive Runge-Kutta schemes for convection-diffusion-reaction equations. *Applied Numerical Mathematics*, 44(1-2):139–181, 2003. doi: 10.1016/s0168-9274(02)00138-1.

[26] C. A. Kennedy and M. H. Carpenter. Diagonally implicit runge–kutta methods for ordinary differential equations: A review. Technical Report NASA/TM 2016-219173, NASA, 2016.

[27] B. Klein, F. Kummer, M. Keil, and M. Oberlack. An extension of the SIMPLE based discontinuous Galerkin solver to unsteady incompressible flows. *International Journal for Numerical Methods in Fluids*, 77(10):571–589, 2015. doi: 10.1002/fld.3994.

[28] G. Kremling and R. Speck. Convergence of multilevel spectral deferred corrections. *Communications in Applied Mathematics and Computational Science*, 16(2):227–265, Nov. 2021. ISSN 1559-3940. doi: 10.2140/camcos.2021.16.227. URL `http://dx.doi.org/10.2140/camcos.2021.16.227`.

[29] A. T. Layton. On the efficiency of spectral deferred correction methods for time-dependent partial differential equations. *Appl. Numer. Math.*, 59(7):1629–1643, July 2009. ISSN 0168-9274. doi: 10.1016/j.apnum.2008.11.004. URL `https://doi.org/10.1016/j.apnum.2008.11.004`.

[30] A. T. Layton and M. L. Minion. Implications of the choice of quadrature nodes for Picard integral deferred corrections methods for ordinary differential equations. *BIT Numerical Mathematics*, 45(2):341–373, 2005. doi: 10.1007/s10543-005-0016-1.

[31] M. Minion. A hybrid parareal spectral deferred corrections method. *Communications in Applied Mathematics and Computational Science*, 5(2):265 – 301, 2010. doi: 10.2140/camcos.2010.5.265. URL `https://doi.org/10.2140/camcos.2010.5.265`.

[32] M. L. Minion. Semi-implicit spectral deferred correction methods for ordinary differential equations. *Communications in Mathematical Sciences*, 1(3):471–500, 2003. doi: 10.4310/cms.2003.v1.n3.a6.

[33] B. W. Ong and R. J. Spiteri. Deferred correction methods for ordinary differential equations. *Journal of Scientific Computing*, 83(3), 2020. doi: 10.1007/s10915-020-01235-8.

[34] Y. Pan, Z.-G. Yan, J. Peiró, and S. J. Sherwin. Development of a balanced adaptive time-stepping strategy based on an implicit JFNK-DG compressible flow solver. *Communications on Applied Mathematics and Computation*, 2021. doi: 10.1007/s42967-021-00138-1.

[35] W. Pazner and P.-O. Persson. Stage-parallel fully implicit runge–kutta solvers for discontinuous galerkin fluid simulations. *Journal of Computational Physics*, 335:700–717, 2017. doi: 10.1016/j.jcp.2017.01.050.

[36] P.-O. Persson and J. Peraire. Sub-cell shock capturing for Discontinuous Galerkin methods. In *44th AIAA Aerospace Sciences Meeting and Exhibit*. American Institute of Aeronautics and Astronautics, 2006. doi: 10.2514/6.2006-112.

[37] R. Schöbel and R. Speck. PFASST-ER: combining the parallel full approximation scheme in space and time with parallelization across the method. *CoRR*, abs/1912.00702, 2019. URL `http://arxiv.org/abs/1912.00702`.

[38] J. Schütz and D. C. Seal. An asymptotic preserving semi-implicit multiderivative solver. *Applied Numerical Mathematics*, 160:84–101, 2021. doi: 10.1016/j.apnum.2020.09.004.

[39] C.-W. Shu and S. Osher. Efficient implementation of essentially non-oscillatory shock-capturing schemes. *Journal of Computational Physics*, 77(2):439–471, 1988. doi: 10.1016/0021-9991(88)90177-5.

[40] G. A. Sod. A survey of several finite difference methods for systems of nonlinear hyperbolic conservation laws. *Journal of Computational Physics*, 27(1):1–31, 1978. doi: 10.1016/

0021-9991(78)90023-2.

[41] R. Speck. Parallelizing spectral deferred corrections across the method, 2017. URL https://arxiv.org/abs/1703.08079.

[42] R. Speck, D. Ruprecht, M. Emmett, M. Minion, M. Bolten, and R. Krause. A multi-level spectral deferred correction method. *BIT Numerical Mathematics*, 55(3):843–867, Aug. 2014. ISSN 1572-9125. doi: 10.1007/s10543-014-0517-x. URL http://dx.doi.org/10.1007/s10543-014-0517-x.

[43] J. Stiller. A spectral deferred correction method for incompressible flow with variable viscosity. *Journal of Computational Physics*, 423:109840, 2020. doi: 10.1016/j.jcp.2020.109840.

[44] J. Stiller. Stable semi-implicit sdc methods for conservation laws. *Journal of Scientific Computing*, 2025. doi: 10.1007/s10915-025-02857-6. URL https://doi.org/10.1007/s10915-025-02857-6.

[45] M. Tavelli and M. Dumbser. Arbitrary high order accurate space–time discontinuous Galerkin finite element schemes on staggered unstructured meshes for linear elasticity. *Journal of Computational Physics*, 366:386–414, 2018. doi: 10.1016/j.jcp.2018.03.038.

[46] G. Čaklović, T. Lunet, S. Götschel, and D. Ruprecht. Improving efficiency of parallel across the method spectral deferred corrections, 2024. URL https://arxiv.org/abs/2403.18641.

Appendix A. Equivalence of incremental and non-incremental two-level Spectral Deferred Correction

Consider $M_l = 2$, denote $\boldsymbol{f}_{l,i}^{k-1} = \boldsymbol{f}(\boldsymbol{u}_{l,i}^{k-1}, t_{l,i})$. Non-incremental MLSDC becomes

$$\boldsymbol{u}_{l,1}^{k} = \boldsymbol{u}_{l,0}^{k} + \Delta t \sum_{i=1}^{M_l} w_{l,i1}^{0\mathrm{N}} \boldsymbol{f}_{l,i}^{k-1} + \boldsymbol{g}_{l,1}^{0\mathrm{N}} + \boldsymbol{H}_{l,1}^{k} - \boldsymbol{H}_{l,1}^{k-1} \tag{71a}$$

$$\boldsymbol{u}_{l,2}^{k} = \boldsymbol{u}_{l,0}^{k} + \Delta t \sum_{i=1}^{M_l} w_{l,i2}^{0\mathrm{N}} \boldsymbol{f}_{l,i}^{k-1} + \boldsymbol{g}_{l,2}^{0\mathrm{N}} + \left(\boldsymbol{H}_{l,1}^{k} + \boldsymbol{H}_{l,2}^{k}\right) - \left(\boldsymbol{H}_{l,1}^{k-1} + \boldsymbol{H}_{l,2}^{k-1}\right) \tag{71b}$$

and incremental MLSDC

$$\boldsymbol{u}_{l,1}^{k} = \boldsymbol{u}_{l,0}^{k} + \Delta t \sum_{i=1}^{M_l} w_{l,i1}^{\mathrm{NN}} \boldsymbol{f}_{l,i}^{k-1} + \boldsymbol{g}_{l,1}^{\mathrm{NN}} + \boldsymbol{H}_{l,1}^{k} - \boldsymbol{H}_{l,1}^{k-1} \tag{72a}$$

$$\boldsymbol{u}_{l,2}^{k} = \boldsymbol{u}_{l,1}^{k} + \Delta t \sum_{i=1}^{M_l} w_{l,i2}^{\mathrm{NN}} \boldsymbol{f}_{l,i}^{k-1} + \boldsymbol{g}_{l,2}^{\mathrm{NN}} + \boldsymbol{H}_{l,2}^{k} - \boldsymbol{H}_{l,2}^{k-1}. \tag{72b}$$

Using the relation between $\underline{w}_l^{\mathrm{NN}}$ and $\underline{w}_l^{0\mathrm{N}}$ the latter can be rewritten to

$$\boldsymbol{u}_{l,1}^{k} = \boldsymbol{u}_{l,0}^{k} + \Delta t \sum_{i=1}^{M_l} w_{l,i1}^{0\mathrm{N}} \boldsymbol{f}_{l,i}^{k-1} + \boldsymbol{g}_{l,1}^{\mathrm{NN}} + \boldsymbol{H}_{l,1}^{k} - \boldsymbol{H}_{l,1}^{k-1} \tag{73a}$$

$$\boldsymbol{u}_{l,2}^{k} = \boldsymbol{u}_{l,0}^{k} + \Delta t \sum_{i=1}^{M_l} w_{l,i2}^{0\mathrm{N}} \boldsymbol{f}_{l,i}^{k-1} + \left(\boldsymbol{g}_{l,1}^{\mathrm{NN}} + \boldsymbol{g}_{l,2}^{\mathrm{NN}}\right) + \left(\boldsymbol{H}_{l,1}^{k} + \boldsymbol{H}_{l,2}^{k}\right) - \left(\boldsymbol{H}_{l,1}^{k-1} + \boldsymbol{H}_{l,2}^{k-1}\right). \tag{73b}$$

Hence, equivalence requires

$$\boldsymbol{g}_{l,1}^{0\mathrm{N}} = \boldsymbol{g}_{l,1}^{\mathrm{NN}} \tag{74a}$$

$$\boldsymbol{g}_{l,2}^{0\mathrm{N}} = \boldsymbol{g}_{l,1}^{\mathrm{NN}} + \boldsymbol{g}_{l,2}^{\mathrm{NN}} \tag{74b}$$

or, more generally

$$\underline{g}_l^{0\mathrm{N}} = \underline{C}_l^{0\mathrm{N}}\, \underline{g}_l^{\mathrm{NN}}. \tag{75}$$

Appendix B. Single-level stability and accuracy

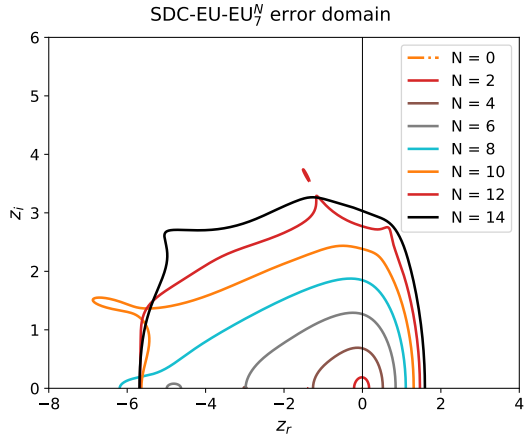

(a) Single-level SDC$_7^N$ with IMEX Euler (corresponds to level 3 MLSDC)

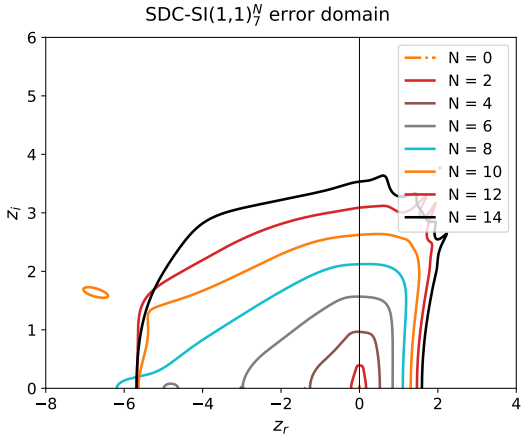

(b) Single-level SDC$_7^N$ with SI(1,1) (corresponds to level 3 MLSDC)

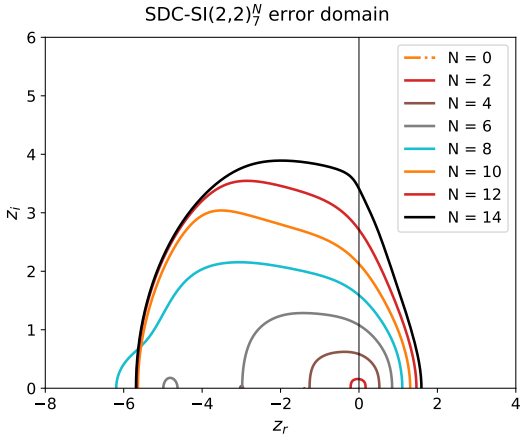

(c) Single-level SDC$_7^N$ with SI(2,2) (corresponds to level 3 MLSDC)

Figure 15. Accuracy curves ($\varepsilon = 10^{-6}$) for single-level SDC methods with RR points and different time integrators shown after each sweep

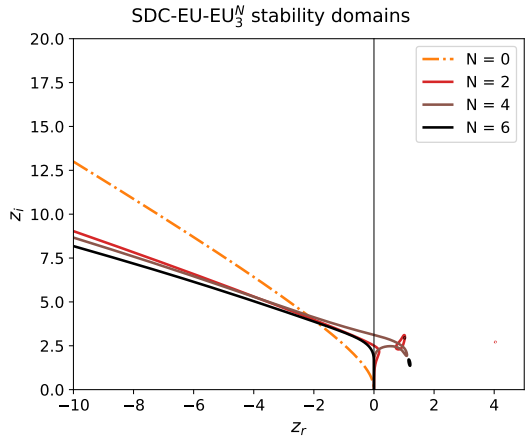

(a) Single-level SDC$_3^N$ with IMEX Euler (corresponds to level 1 MLSDC)

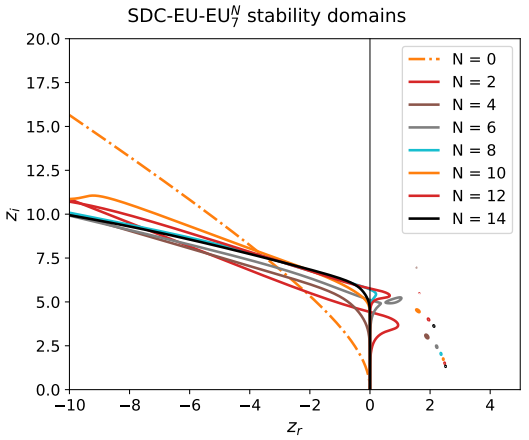

(b) Single-level SDC$_7^N$ with IMEX Euler (corresponds to level 3 MLSDC)

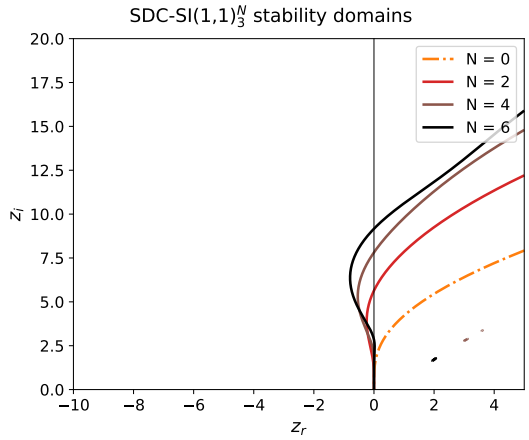

(c) Single-level SDC$_3^N$ with SI(1,1) (corresponds to level 1 MLSDC)

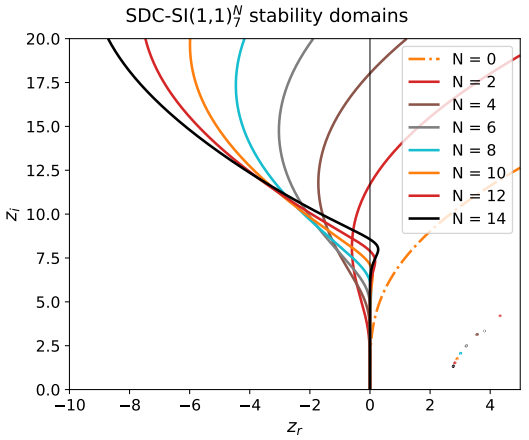

(d) Single-level SDC$_7^N$ with SI(1,1) (corresponds to level 3 MLSDC)

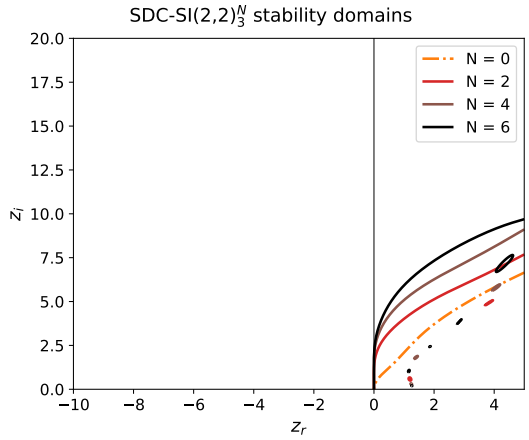

(e) Single-level SDC$_3^N$ with SI(2,2) (corresponds to level 1 MLSDC)

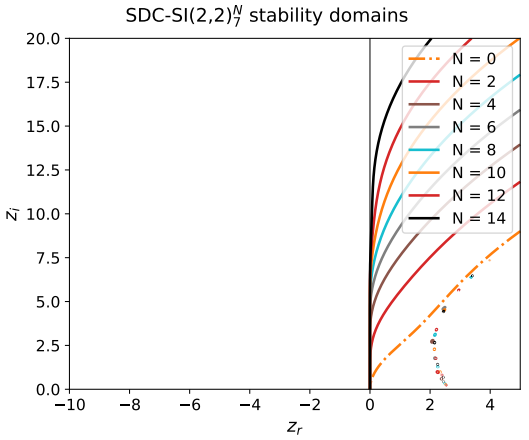

(f) Single-level SDC$_7^N$ with SI(2,2) (corresponds to level 3 MLSDC)

Figure 16. Neutral stability curves for single-level SDC methods with RR points and different time integrators shown after each second sweep